Australian Government
Department of Defence
Defence Science and
Technology Organisation

Non-destructive Evaluation of Aircraft Structural Components and Composite Materials at DSTO Using Sonic Thermography

Kelly A. Tsoi and Nik Rajic

Air Vehicles Division

Defence Science and Technology Organisation

DSTO–TN–0986

ABSTRACT

This report outlines the results of a series of non-destructive evaluations using sonic thermography. It examines the detection of closed cracks, delaminations, impact damage and other defects in a variety of structural components and composite materials used in aircraft structures. The results confirm the efficacy of the technique and highlight its potential to fill some of the capability gaps that currently exist in relation to challenging non-destructive inspection problems.

APPROVED FOR PUBLIC RELEASE

Published by

DSTO Defence Science and Technology Organisation
506 Lorimer St,
Fishermans Bend, Victoria 3207, Australia

Telephone: (03) 9626 7000
Facsimile: (03) 9626 7999

© *Commonwealth of Australia 2011*
AR No. AR-014-921
February 2011

The images in the printed version are subject to the limitations of the printing process and as such are best resolved by viewing the electronic version of this report.

APPROVED FOR PUBLIC RELEASE

Non-destructive Evaluation of Aircraft Structural Components and Composite Materials at DSTO Using Sonic Thermography

Executive Summary

The rapid rate of advancement in materials and manufacturing technologies ensures an ongoing requirement for improved non-destructive evaluation (NDE) techniques. To cater for known shortfalls in contemporary NDE capability, damage tolerance assessments which underpin the structural airworthiness of many air platforms are often made deliberately conservative. Thus, a strong motivation exists for the development of enhanced inspection capabilities that may offer a basis for more efficient structural management.

A strong impetus already exists in relation to the inspection of tightly closed cracks in metallic components and kissing bonds in composite structures which are often difficult to detect using conventional NDE methodologies. Sonic thermography shows some promise in these and other difficult applications. It involves injecting a specimen with high frequency acoustic waves. These waves radiate through the specimen, interacting with flaws to produce lateral relative motion at the flaw surfaces. In the presence of a compressive stress this motion gives rise to frictional heating which in turn produces a thermal signature.

This report documents some of the applications of a sonic thermographic facility developed by the Defence Science and Technology Organisation (DSTO) to the detection of defects in a variety of aircraft structural components and composite materials. The results confirm that sonic thermography has the potential to assist the Australian Defence Force (ADF) in solving some difficult inspection problems and could therefore help in reducing through life support costs for aircraft.

THIS PAGE IS INTENTIONALLY BLANK

Authors

Kelly A. Tsoi
Air Vehicles Division

Kelly Tsoi completed a BSc. (Hons.) in Physics at The University of Melbourne in 1995. She commenced work in the Airframes and Engines Division of the Aeronautical and Maritime Research Laboratory in 1996 and has worked on methods of fatigue life enhancement using smart materials. In 1998 she commenced studies at The University of Sydney and Katholieke Universitait Leuven, Belgium in shape memory alloys and their composites, which led to the completion of a PhD in 2002. She is currently a Research Scientist in the Smart Structures and Advanced Diagnostics group of the Air Vehicles Division involved in the development of active thermographic techniques for non-destructive evaluation and the development of in situ structural health monitoring techniques.

Nik Rajic
Air Vehicles Division

Nik Rajic received a B. Eng. (Hons.) in Mechanical Engineering from the University of Melbourne in 1989. He joined Structures Division at the Aeronautical Research Laboratory in 1991 and in 1992 undertook studies at Monash University which led to the completion of a PhD in 1995. He has since contributed to research on fatigue-life extension techniques, thermoelastic stress analysis, thermoplasticity, thermographic nondestructive evaluation and in situ structural health monitoring techniques based on smart structures principles. He is currently a Senior Research Scientist in the Smart Structures and Advanced Diagnostics group of the Air Vehicles Division.

THIS PAGE IS INTENTIONALLY BLANK

Contents

Glossary **xv**

1 Introduction **1**

2 Experimental Setup **1**

2.1 Acoustic Horn 1

2.2 Infrared Camera 2

2.3 Flash Thermography Inspection 3

2.4 Image Processing 3

3 Detection of Composite Disbonds and Delaminations **3**

3.1 Teflon insert 4

3.2 Thin film insert 5

3.3 Vaseline contamination 12

3.4 Glass reinforced aluminium specimens 16

3.5 Lapjoint specimen 16

3.6 F-111C: A15-5 lower wing skin section 18

3.7 Mirage III Boron Patch Teardown 23

4 Impact damage detection **25**

4.1 Impact damage in carbon fibre composites 25

4.2 Step lapjoint specimen 26

4.3 Syncore specimens 29

4.4 Detection of impact damage and artificial inclusions in composite panels. 30

5 I-beam inspection: geometrically challenging structures **36**

6 Crack detection beneath CBRs **38**

7 Cracking in an F-16 main wheel rim **44**

7.1 Effect of horn tip position on IR signature 45

7.2 Effect of power level and insonification time on IR signature 46

7.3 Summary of results 48

7.3.1 Stem 1 48

7.3.2 Stem 2 48
7.3.3 Stem 3 49
7.3.4 Stem 4 49
7.3.5 Stem 5 49

8 General Discussion and Conclusions 51

9 Acknowledgements 52

References 53

Figures

1 Experimental setup showing the specimen, acoustic horn and infrared camera. 2

2 Dimensions and layup of a C/Ep composite specimen with embedded teflon inserts. Measurements are in mm. 4

3 From top to bottom, ST raw, PPT and PCT_2 results and flash PPT showing signatures from the Teflon inserts. 6

4 (a) Diagram of the insert positions embedded in the mid plane, 50% of the total thickness of the laminate and in the near surface, 15% of the total thickness, (b) photograph of the specimen, the outline in red shows the inspection area and (c) through-transmission ultrasound image showing insert locations in specimens A, B and C, from the reverse side of the specimens, as indicated (courtesy CRC-ACS). 7

5 ST inspection of the thin film insert specimens from front face. Specimens A, B and C are indicated, and the PPT and PCT_{1-5} results, are shown. The defect positions for specimens A and B are shown to the right of the thermographs. 9

6 FT inspection of the thin film insert specimens. Specimens A, B and C are indicated, and the PPT, and PCT results for modes 2 and 4, are shown. The defect positions for specimens A and B are shown to the right of the thermographs. 10

7 ST inspection of the reverse face of the thin film delamination specimens showing PCT_2 and PCT_4 results for specimen A and PCT_4 and PCT_5 results for specimen B as indicated. The defect positions for specimens A and B are shown to the right of the thermographs. 11

8 Diagram of the skin-frame flange panel showing flange 1 as the bonded and riveted frame and flange 2 as the bonded frame. 12

9 (a) Damage map, (b) ST result (PCT_3) and (c) FT result of specimen 1. The results shown in (b) and (c) are of the respective thermographs which have been superimposed with a photograph of the panel. In (a) the coloured circles correspond to the vaseline contamination in the bondline, red crosses indicate impact fractures and areas marked by the red outline indicate damage disclosed by C-scans. In (b) the arrow indicates vibrational mode patterns due to anelastic heating. Note that the blue circles in (c) (an example of which is indicated by the arrow) are markers used for alignment of the thermographic images. 14

10 (a) Damage map, (b) ST result (phase) and (c) FT result for specimen 2. The results shown in (b) and (c) are of the respective thermographs which have been superimposed with a photograph of the panel. In (a) the coloured circles correspond to the vaseline contamination in the bondline, red crosses indicate impact fractures and areas marked by the red outline indicate damage disclosed by C-scans. In (b) the arrows indicate vibrational mode patterns due to anelastic heating. Note that the blue circles in (c) (an example of which is indicated by the arrow) are markers used for alignment of the thermographic images. 15

11 Sonic PPT (left) and PCT_2 (right) results of glass reinforced aluminium specimens with embedded Teflon inserts with varying diameters of (a-b) 40, (c-d) 80 and (e-f) 100 mm respectively. (g-h) correspond to a reference specimen. . 17

12 PPT (left) and PCT_2 (right) results of glass reinforced aluminium specimens with embedded Teflon inserts captured with the inserts below the E-glass-fibre (a-b) and above the E-glass-fibre (c-d). 18

13 From top to bottom, photograph of lapjoint side A, corresponding PPT result, photograph of lapjoint side B and its corresponding PPT result. 19

14 Photograph of the experimental setup showing the specimen, acoustic horn and thermal camera. 20

15 (a)Photograph of the LWS fragment 12W951A1 indicating region of interest. (b) Raw ST image showing darkened regions indicating elevated heat production and possible disbonds. 20

16 (a) PPT and (b) PCT results elucidating the disbond in regions A and B. Different grey scales were used in order to accentuate the flaw regions. . . . 21

17 Comparison of sonic PPT, flash PPT and C-scan results, respectively showing the disbonds in regions A and B. 21

18 Photograph of fragment 12W951X, indicating regions of interest, D and E and point of insonification. 21

19 (a) and (b) are the sonic PCT_2 results of region D and (c) the corresponding flash PPT result of the same region (circled) and (d) and (e) are the sonic PCT_2 results of region E and (f) the corresponding flash PPT result. 22

20 Diagram of the experimental setup used for ST of the Mirage III boron patches. 23

21 Photograph of a typical Mirage III boron patch under investigation. 24

22 Results for (a) flash PPT (b) sonic PCT_2 (c) BaNDIcoot with peak index set at 4% and 9-15 kHz and (d)BaNDIcoot with peak index set at 2% and 25-35 kHz. The defect indications are circled in pink. An example of the pullout stub size is shown in (b) as a white circle. 25

23 (a)Photograph of the impact damaged regions of the composite specimen; impact regions are indicated by the circles. ST (b) raw, (c) PPT and (d) PCT_2 results and (e) flash PPT result of the impact damaged regions of the composite specimen. 27

24 Photograph of the single impact specimen with the impact region indicated by the square. 27

25 The ST (a) PPT and (b) PCT_3 results and the (c) flash PPT result of the impact damaged region of the composite specimen. 28

26 Photograph of the step lapjoint specimen showing the impact region and the insonification point. The bottom left image is the sonic PCT_2 result and the bottom right image is a flash PPT result of the damaged region. 28

27 Raw ST (left) and PCT_2 (right) results, respectively, for Syncore specimens A and B. 29

28 (a) Damage map, (b) profile image of layup, (c) sonic and (d) flash thermographs showing the four quadrants of specimen 1A and the corresponding damage locations. The 'U' and 'P' refer to the damage locations on the unpainted and painted side of the specimen, respectively. *(Specimen layout courtesy CRC-ACS.)* 31

29 (a) Damage map, (b) profile image of layup, (c) sonic and (d) flash thermographs showing the four quadrants of specimen 1B and the corresponding damage locations. *(Specimen layout courtesy CRC-ACS.)* 32

30 (a) Damage map, (b) profile image of layup, (c) sonic and (d) flash thermographs showing the four quadrants of specimen 2A and the corresponding damage locations. *(Specimen layout courtesy CRC-ACS.)* 33

31 Profile image of the layup of specimen 2A *(courtesy CRC-ACS)*. 34

32 (a) Damage map, (b) profile image of layup, (c) sonic and (d) flash thermographs showing the four quadrants of specimen 2B and the corresponding damage locations. *(Specimen layouts courtesy CRC-ACS.)* 35

33 Experimental setup for investigation of I-beam defects, showing thermal camera, acoustic horn and specimen. 36

34 (a) Photograph of I-beam showing the regions of interest, A and B, and (b) the corresponding sonic thermograph. 37

35 Photograph of region B (top) and the sonic PCT_3 results for the damaged area of the I-beam (middle) and the reference specimen (bottom). 37

36 Photograph of the B/Ep patched honeycomb panel showing the dimensions and insonification points. 39

37 FT PPT results of sides A and B of the B/Ep patched honeycomb panel. . . 39

38 ST raw, PPT and PCT_2 results of the B/Ep patched honeycomb panel insonified at point a (indicated in Figure 36). 40

39 ST raw, PPT and PCT_2 results of the B/Ep patched honeycomb panel insonified at point b (indicated in Figure 36). 41

40 ST PPT and PCT_2 results of B/Ep patched honeycomb panel insonified at four locations (a, b, c and d) on side A, as indicated, corresponding to Figure 36. 42

41 (a) and (b) show the ST PCT_2 results of B/Ep patched honeycomb panel insonified on side A at locations a and e, respectively, corresponding to Figure 36. (c) is the cross-correlation result of the two PCT results. 43

42 Photograph of (a) F-16 main wheel rim, the five stems to be inspected are indicated, (b) one of the stems, with the region of interest highlighted by the box and (c) a close up view of the area to be inspected. For this case a visible crack is observable. 44

43 Experimental setup showing painted main wheel rim with the mirror, IR camera and acoustic horn in position. 45

44 Horn tip positions. 46

45 PCT results corresponding to insonification positions (a) 1 and (b) 2 of stem 2. (c) shows a photograph of the region. The parallel lines are used to align the thermal images with the photograph. 46

46 PCT results for stem 1 indicating varying insonification times (1 s, 2 s, 3 s, 4 s) and power levels (50% and 70%). 47

47 Stem 1: photograph and PCT results for the painted (left) and unpainted area (right), respectively. 48

48 Stem 2: photograph and PCT results for the painted (left) and unpainted area (right), respectively. 49

49 Stem 3: photograph and PCT results for the painted (left) and unpainted area (right), respectively. 49

50 Stem 4: photograph and PCT results for the painted (left) and unpainted area (right), respectively. 50

51 Stem 5: photograph and PCT results for the painted (left) and unpainted area (right), respectively. 50

Tables

1 Table showing thin film inserts detected using ST and FT 8

2 Table showing defect size and minimum detectable defect size for IR thermography with respect to the thin film inserts 10

3 Table showing the layup of the received specimens with vaseline disbonds *(Courtesy CRC-ACS)*. 12

4 Comparison of the accuracy of NDI indications. 26

5 Table showing the layup of the received specimens *(courtesy CRC-ACS)*. . . . 30

6 Table showing the energies applied in the impacts on specimens 1A, 1B, 2A and 2B *(courtesy CRC-ACS)*. 30

7 Table showing minimum detectable defect size for IR thermography with respect to the Teflon disbonds in specimen 2A 34

THIS PAGE IS INTENTIONALLY BLANK

Glossary

ADF Australian Defence Force

B/Ep Boron fibre/ Epoxy resin

BVID Barely Visible Impact Damage

C/Ep Carbon fibre/ Epoxy resin

CBR Composite Bonded Repair

CRC-ACS Co-operative Research Centre in Advanced Composite Structures

EMS Electromagnetic Shielding

FML Fibre reinforced Metal Laminates

FT Flash Thermography

IR Infrared

LWS Lower Wing Skin

NDE Non-Destructive Evaluation

NDI Non-Destructive Inspection

PCT Principle Component Thermography

POTS Pull-off Tensile Strength

PPT Pulsed Phase Thermography

SNR Signal to Noise Ratio

ST Sonic Thermography

UT Ultrasonic Testing

1 Introduction

An important element in the effective structural management of aircraft components is the development of non-destructive evaluation (NDE) techniques which enhance and add to the complement of existing techniques. Of particular value is the development of techniques which enable the detection of defects in aircraft structural components which pose an insuperable problem to conventional NDE. Examples of such problematic defects include kissing bonds in composite structures and tightly closed cracks in metallic components. In addition, a capability for monitoring the integrity of composite bonded repairs and the growth of existing cracks in metallic structure beneath such repairs would be of great value.

Sonic thermography (ST), offers good prospects for these and other difficult applications. The technique uses relatively high frequency (typically < 40 kHz) acoustic waves which are introduced into the specimen, using an acoustic horn. The acoustic waves induce lateral motion at the surfaces of crack or delamination type defects, which combined with existing frictional forces produces heat. The measurable manifestation of this heat production is an infrared emission from the surface of the inspected component, which is detected using a thermal imaging system.

Previous investigators [1]-[2] found that for non-resonant specimens, heat was generated at defect sites and, in particular, around large columnar grain boundaries and artificial defects such as fatigue cracks and saw cuts. Tenek and Henneke [3] showed that by exciting a damaged composite specimen the heat generated by defects can be detected using a thermal imaging system. They determined that this heating was primarily due to the presence of mechanical resonance at the delamination faces which generated local heating. By changing the mechanical vibration frequency of the composite panel, the thermal gradients observed faded in and out, depending on the resonance. Zweschper *et al* [4] used a similar method where, instead of using a pulsed excitation, a persistent harmonic source is used and the thermal signal is synchronously averaged. They found that it was very successful in detecting various types of damage including impact and delaminations in composite materials. It also appeared useful in detecting loose rivets in metal plates as well as hidden corrosion.

Since the work of Zweschper, there has been an increased interest in this technique with researchers worldwide developing their own form of the technique.

This technical note summarises the application of a sonic thermographic system developed at the DSTO for the detection of damage in a variety of composite structures, composite bonded repairs and metallic structures, comparing the results of these inspections with those obtained using other NDE methods.

2 Experimental Setup

2.1 Acoustic Horn

The acoustic horn used in the investigations in this report is a commercial ultrasonic plastic welder which operates at a 20 kHz frequency. As the acoustic horn is optimised for welding

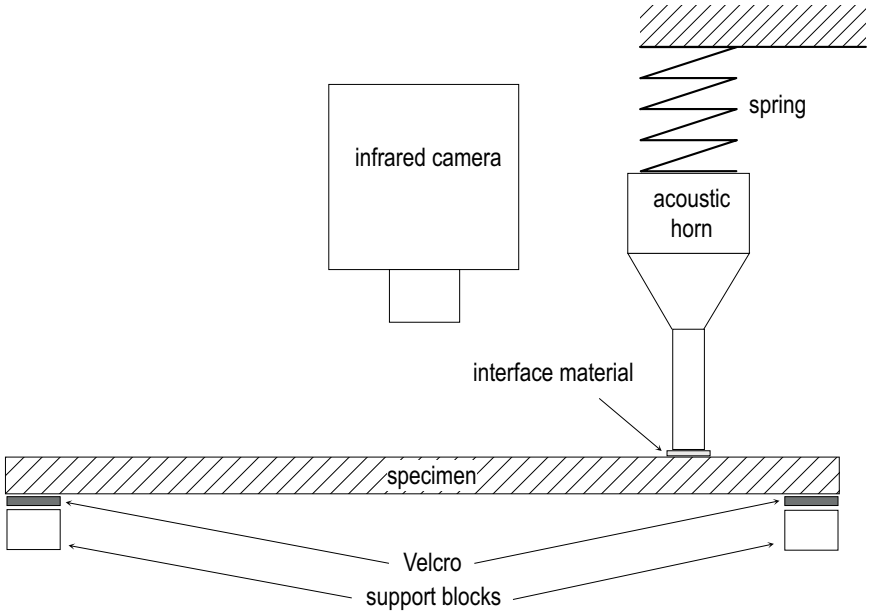

Figure 1: *Experimental setup showing the specimen, acoustic horn and infrared camera.*

plastics it cannot yield optimal performance across the broad range of aircraft structural materials since by matching the impedance at the probe tip to plastics the acoustic energy transfer into other materials, particularly metals, is compromised. Improved transfer can, however, be achieved by introducing a sufficiently compliant material between the probe tip and the test subject [5]. Such an interface is normally also prescribed for the inspection of polymer-composite materials, despite a better impedance match, both to further improve acoustic coupling as well as to protect the object surface from damage. In the DSTO inspection system, the insonification event is synchronised with the infrared image capture system using customised software.

Where appropriate, items were inspected in a specially fabricated rig, as shown schematically in Figure 1. As indicated, specimens were secured to the rig using Velcro, which serves two important purposes. (i) It restrains the object from moving under considerable dynamic excitation from the probe, and (ii) it provides an acoustic energy barrier limiting the amount of energy lost from the sample [6]. A spring was used to maintain a constant force between the specimen and the probe and also serves to restrain chattering of the probe against the sample.

2.2 Infrared Camera

Two infrared cameras were used for the thermal inspections in this report. The first system was a Raytheon Radiance HS. The infrared focal plane array is cryogenically cooled and has 256 x 256 Indium Antimonide (InSb) detector elements with a sensitivity of 20 mK in the operating wavelength band of 3-5 μm. The detectors are operated in snap-shot mode with the integration time and image frame-rate controlled through the software. The frame rate can be varied from a maximum of 140 Hz for a 256 x 256 array to 2 kHz

for a central 64 x 64 sub-array. The second camera, a FLIR SC6000, has an infrared focal plane array with an increased array size of 640 x 512 InSb detector elements and a sensitivity of 15 mK.

For thermographic inspections the subject is typically coated with a high emissivity paint in order to remove background thermal reflections which could cloud the results, and to improve thermal emissions from the subject. Most carbon-epoxy laminates have a good IR emissivity, however where this was not the case the subject was coated with a thin layer of paint prior to inspection.

2.3 Flash Thermography Inspection

For many of the examples considered in this report an ST inspection has been supplemented with an inspection using flash thermography (FT). In FT the infrared camera is mounted to an inspection head (developed by DSTO) containing linear xenon flash tubes powered by a 6 kJ high voltage capacitor unit. The lamps are triggered remotely through custom software, which also synchronises data capture through the infrared camera. Further detail about the system and process of FT can be found in [7].

2.4 Image Processing

Infrared imaging has an inherently poor signal to noise ratio (SNR) compared to visible imaging and profits greatly from various signal enhancement techniques. Two types of postprocessing were applied to the ST data: pulsed phase thermography (PPT) [8] and principal component thermography (PCT) [9]. PPT transforms the frame sequence obtained from the infrared camera into a map of the spatial variation of time delays at a particular temporal frequency, thus time varying components of the signal, generally related to regions of heat disturbance, are selectively enhanced. PCT is similar to the extent that it also maps the raw data to a set of basis functions but instead of using an analytical and oscillatory set of basis functions, as in the Fourier transform, it employs an empirically derived basis, called empirical orthogonal functions or modes. It is a conceptually more attractive approach in that it avoids the rather arbitrary assignment of a specific functional form to the basis, and is found to deliver better SNR than PPT in many situations. In this report the subscripts assigned to PCT results denote the order of the mode. The raw FT data was post processed using PPT.

3 Detection of Composite Disbonds and Delaminations

The earliest possible detection of damage and degradation in composite bonded repairs (CBRs) is always preferred, particularly where flight critical structure is involved. The inspection of CBRs, however, can pose some difficulty particularly where the patch is thick and kissing bonds exist. There are several standard techniques which can be used to detect defects in composite structures including ultrasonics, thermography, acoustic

emission and SPATE to name a few (details of these techniques can be found in [10]). No single technique has proven to be reliable under all possible inspection conditions.

As already remarked, kissing bonds in composite structures pose a significant problem for current NDE techniques. The definition of a kissing bond varies. Examples of kissing bonds include a crack under normal compressive pressure [11], an adhesive disbond between two surfaces, where the surfaces are still connected, through solid-solid contact under compression or by the interface being contaminated by a thin liquid layer [12], or in a situation where very weak, 'sticky' bonding exists, but there is no strength in the bond [13]. If the two surfaces are in a region of compression it can be almost impossible to detect with current NDE techniques. ST is intuitively a strong candidate for the inspection of disbonding and delamination, and in particular kissing bonds, since these types of flaws involve two surfaces in close contact, producing an environment conducive to frictional heating during insonification. The definition of a kissing bond used in this investigation is a region of failed adhesion where compressive stresses maintain closure of the interface and thereby partially and in some cases completely obscure the defect to conventional non-destructive inspection methods.

Several examples have been investigated in order to show the ability of ST to detect such defects. These include: (i) composite specimens with (a) Teflon, (b) Airtec Tooltec film and (c) vaseline inserts which are used to simulate a disbond within a composite patch, (ii) fibre reinforced metal laminate specimens with embedded Teflon inserts of three different diameters, (iii) a lapjoint specimen containing a delamination, (iv) an example of disbonding in the F-111C lower wing skin (LWS) CBR and (v) detection of weak bonding in the adhesive layer of Mirage III boron CBRs.

3.1 Teflon insert

A carbon-fibre/epoxy-resin (C/Ep) system (AS4/3501-6) was used to make up a 50 ply, 6.7 mm thick specimen with a lay-up of $[+45_2/-45_2/0_4/+45_2/-45_2/0_4/+45_2/-45_2/0_4/90]_s$. To simulate a delamination in the structure, teflon film discs were inserted between plies 12-13 and 13-14, during layup, as shown in Figure 2.

The specimen was insonified for 6 s at an arbitrary location close to the specimen edge. The acoustic horn was operated at 500 W and thermal image capture occurred at 10 Hz over 30 frames corresponding to an inspection time of 30 s. The first three images of

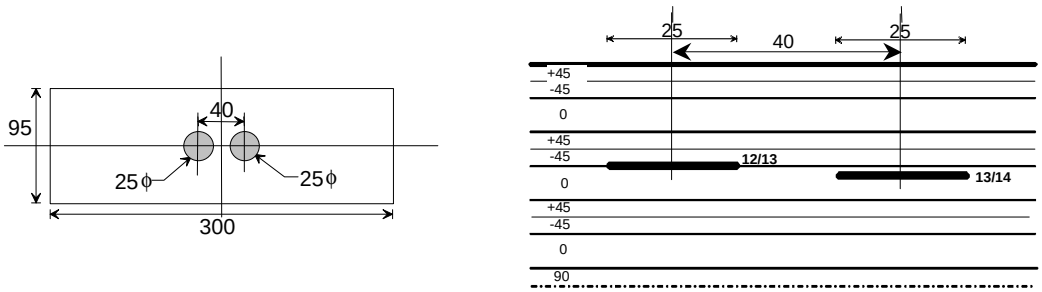

Figure 2: *Dimensions and layup of a C/Ep composite specimen with embedded teflon inserts. Measurements are in mm.*

Figure 3 show the raw, PPT and PCT_2 results, respectively, obtained from the inspection. The Teflon inserts are clearly visible. The insert on the right produces the weaker of the two indications. This is anticipated since the greater sub-surface depth promotes increased heat conduction and thereby more signal attenuation. The last image in Figure 3 shows the corresponding flash PPT result. The two inserts are observable but there is less definition when compared to the sonic PPT result. Additionally, no clear difference is apparent between the two inserts that might indicate the insertion depth. This however stems from the image processing methodology used rather than flash inspection in general, since the primordial time-evolution data will contain information pertaining to defect depth.

3.2 Thin film insert

A set of three 6 mm thick specimens were manufactured from a toughened epoxy/ carbon laminate (aerospace grade) via a liquid moulding process.[1] In order to simulate delamination type defects, 0.16 mm thick Airtec Tooltec PTFE film (similar to Teflon) was embedded with different shapes and sizes within the ply layup as shown in Figure 4(a). The first group of inserts (1, 3, 5, 7 and 9) were located at a depth of 15% of the total thickness and the second group (2, 4, 6, 8 and 10) were located in the mid-plane of the laminated specimen (50% of the total thickness). The inserts were spaced uniformly along the length of the specimen. Table 2 shows the dimensions of the inserts. Two specimens were embedded with the thin film inserts (specimens A and B), whilst a third specimen (C) was used as a reference. Figure 4(b) shows a photograph of one of the specimens and Figure 4(c) is the through-transmission ultrasound image showing the precise locations of the delaminations. The acoustic horn was operated at 555 W for a duration of 1.0 s and thermal image capture occurred at 50 Hz over 300 frames.

Figure 5 shows the PPT and PCT results for the ST inspection of specimens A, B and C. The PCT results show the first five modes. The PPT results for specimens A and B show strong indications for inserts located at a depth of 15% below the surface . For both specimens A and B, all modes show indications of inserts 1 and 7. Modes 2, 3, and 4 (PCT_2, PCT_3 and PCT_4) show indications of the inserts embedded at 15%. For the inserts embedded in the midplane, there appears to be no indication for specimen A, however for specimen B defects 2, 4 and 8 are observable in PCT_5. Specimen C shows vibration modes set up within the specimen due to the acoustic excitation. These are distinguished from structural defects by the distinctly periodic pattern of the signature, which effectively maps the anelastic strain amplitude in the specimen. Interestingly, while specimen B produces a modal pattern similar to that of specimen C, specimen A yields a different pattern. This could be a result of slight variations in laminate thickness, variations in the defect geometry or acoustic horn position during insonification.

[1]Specimens provided by the Co-operative Research Centre in Advanced Composite Structures (CRC-ACS)

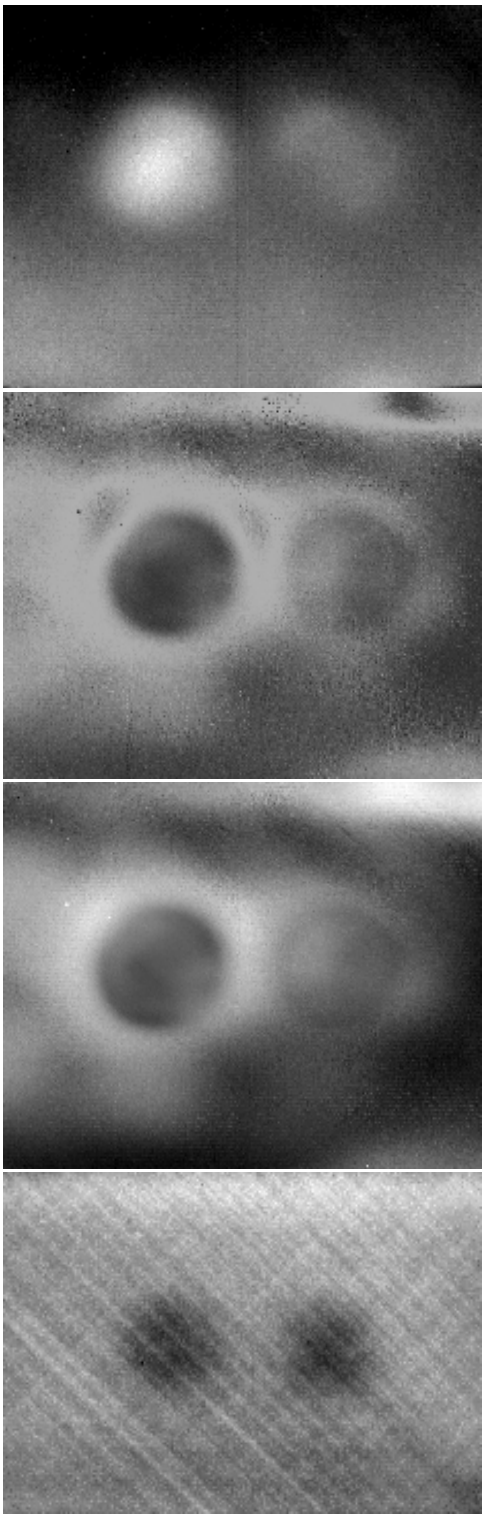

Figure 3: *From top to bottom, ST raw, PPT and PCT_2 results and flash PPT showing signatures from the Teflon inserts.*

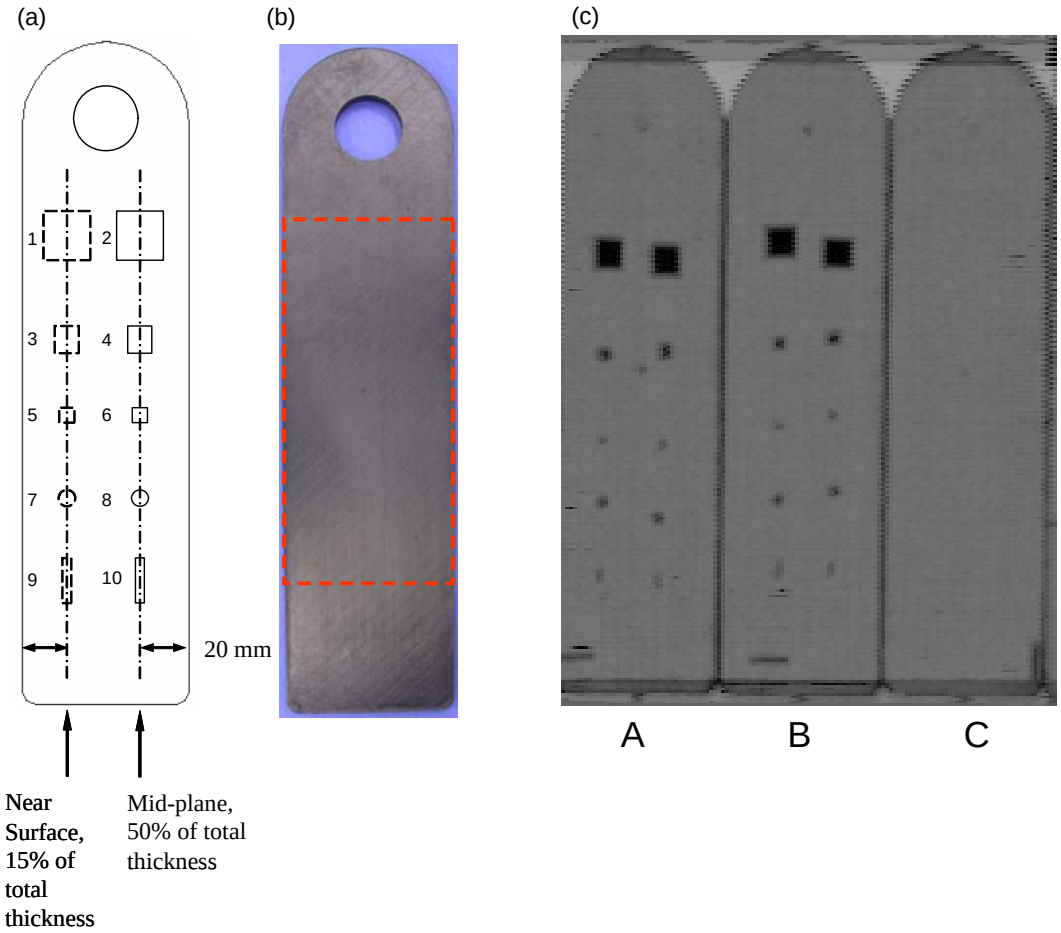

Figure 4: *(a) Diagram of the insert positions embedded in the mid plane, 50% of the total thickness of the laminate and in the near surface, 15% of the total thickness, (b) photograph of the specimen, the outline in red shows the inspection area and (c) through-transmission ultrasound image showing insert locations in specimens A, B and C, from the reverse side of the specimens, as indicated (courtesy CRC-ACS).*

Table 1: *Table showing thin film inserts detected using ST and FT*

	specimen A		specimen B	
	Detectable?		Detectable?	
Defect	ST	FT	ST	FT
1	✓	✓	✓	✓
2	×	✓	✓	×
3	✓	✓	✓	✓
4	×	×	✓	×
5	✓	✓	✓	✓
6	×	×	×	×
7	✓	✓	✓	✓
8	×	×	✓	×
9	na	×	✓	×
10	na	×	×	×

Figure 6 shows the results of FT inspections of the same specimens. An acquisition rate of 50 Hz over 300 frames was used. The PPT, PCT_2 and PCT_4 results show indications of inserts 1, 3, 5 and 7 for both specimens A and B. For specimen A the PPT and PCT_2 results give good indications of insert 2. Table 1 shows the detectability of the inserts using ST and FT.

The difficulty in detecting the smaller inserts at a depth 15% below the surface (5, 7 and 9) and the majority of the inserts embedded in the midplane of the specimen (4, 6, 8 and 10) is due, in part, to the fundamental sensitivity limitations of thermographic techniques. According to Maldague [14], a rough rule of thumb for a defect to be detectable using active thermography is that its effective radius should be at least as large as its depth beneath the surface. A summary of the insert sizes for the case in hand, based on this general rule, is shown in Table 2, where the relevant lateral dimension is taken to be the effective radius. The 'depth' shown in Table 2 gives the minimum depth at which the inserts in these specimens should be detectable. Based on these results, it can be seen that the inserts embedded at a depth of 15% below the surface should be detectable, and the PPT results for the ST and FT inspections substantiate this. For an embedment depth of 50%, the two largest defects (2 and 4) should be observable, whilst the rest of the defects are below the detection limit. In the ST inspections of specimen B it is possible to detect insert 2, as can be observed in the PPT result and all modes of the PCT results, and insert 4 is observable in the PCT_5 result. Interestingly, insert 8 is just observable in PCT_5, even though it is below the minimum detectable limit given by Maldague [14].

Figure 7 shows the ST inspection of the reverse side of the specimens, in which defects located 0.9 mm beneath the surface are now located at 5.1 mm below the surface. Only PCT_2 and PCT_4 for specimen A and PCT_4 and PCT_5 for specimen B are shown. From these results it can be observed that for specimen A, defects 2 and 6, in the midplane, which were previously not observable, are now detectable in PCT_2 and defect 2 alone in PCT_4. For specimen B, defect 1, at 5.1 mm and defect 2, at 3 mm below the surface, are observable in the PCT_4 and only defect 2 is observable in the PCT_5 results.

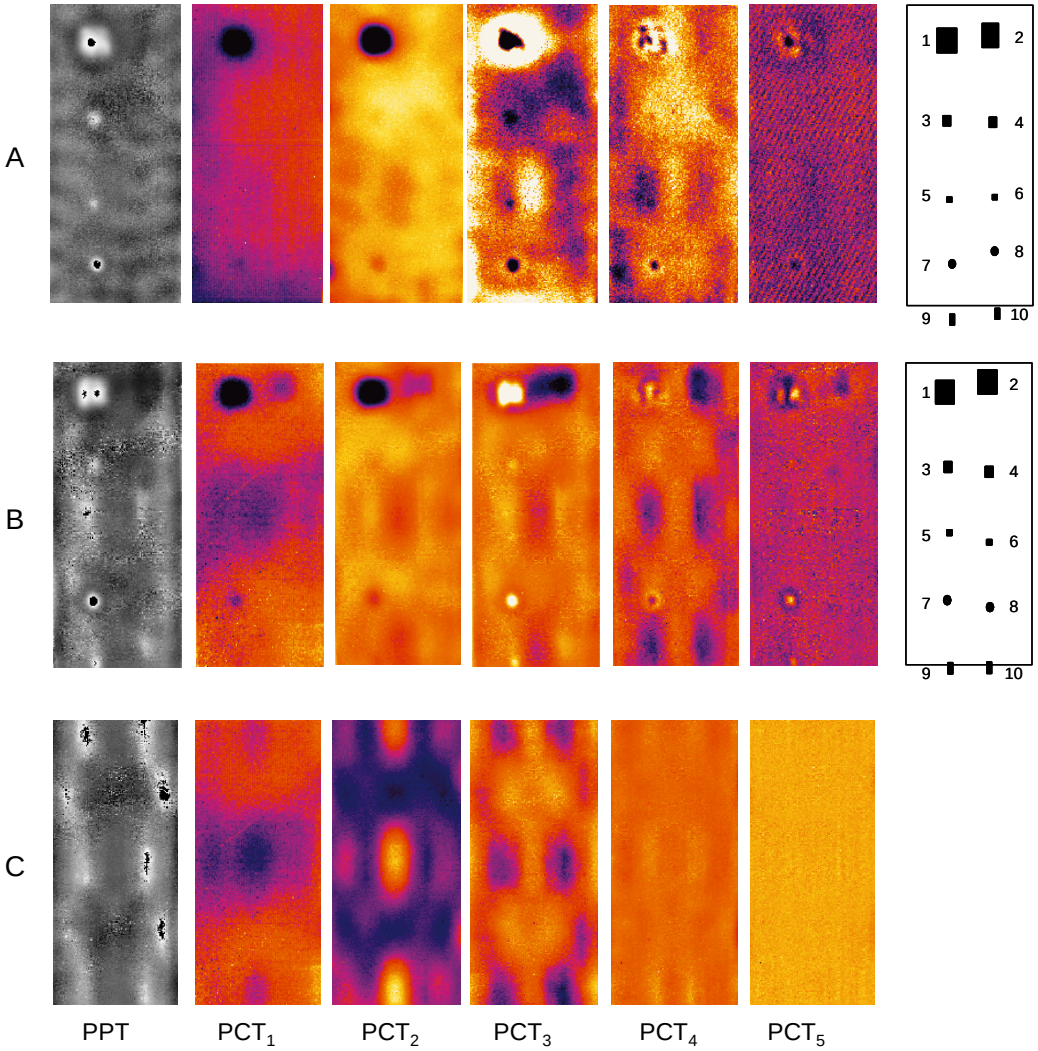

Figure 5: *ST inspection of the thin film insert specimens from front face. Specimens A, B and C are indicated, and the PPT and* PCT_{1-5} *results, are shown. The defect positions for specimens A and B are shown to the right of the thermographs.*

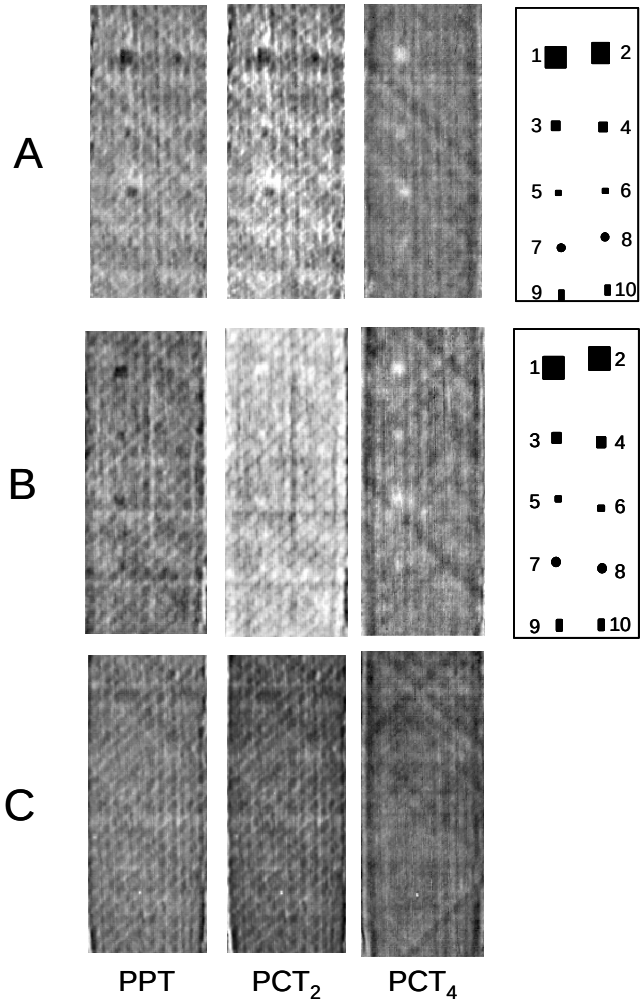

Figure 6: *FT inspection of the thin film insert specimens. Specimens A, B and C are indicated, and the PPT, and PCT results for modes 2 and 4, are shown. The defect positions for specimens A and B are shown to the right of the thermographs.*

Table 2: *Table showing defect size and minimum detectable defect size for IR thermography with respect to the thin film inserts*

Insert #	Defect size, D (mm)	D/2 (mm)	Depth 0.9 (15%) (mm)	Depth 3 (50%) (mm)	Depth 5.1 (75%) (mm)
1 & 2	12.7 x 12.7	6.35	✓	✓	✓
3 & 4	6.35 x 6.35	3.175	✓	✓	×
5 & 6	3.175 x 3.175	1.59	✓	×	×
7 & 8	⌀3	1.5	✓	×	×
9 & 10	2 x 5	1	✓	×	×

'Insert #' corresponds to the insert label shown in Figure 4.
'Defect size' shows the dimensions of the embedded thin film inserts.
'Depth' indicates the depth of the embedded defect and whether it is detectable based on the empirical rule given by Maldague, [14].

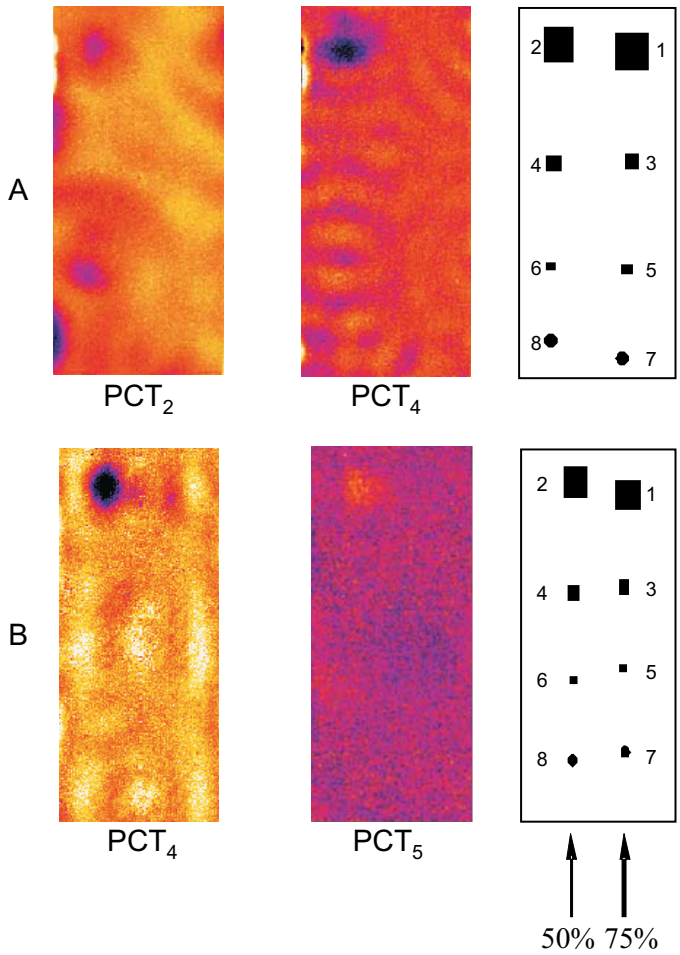

Figure 7: *ST inspection of the reverse face of the thin film delamination specimens showing PCT_2 and PCT_4 results for specimen A and PCT_4 and PCT_5 results for specimen B as indicated. The defect positions for specimens A and B are shown to the right of the thermographs.*

Table 3: *Table showing the layup of the received specimens with vaseline disbonds (Courtesy CRC-ACS).*

Specimen 1	Skin-frame panel consisting of a 9-ply skin with layup of [45/0/0/-45/0/-45/0/0/45] and two simulated frame flange's consisting of a 12-ply layup of [45/02/-45/04/-45/02/45]
Specimen 2	Skin-frame panel consisting of a 9-ply skin with layup of [45/0/0/-45/0/-45/0/0/45] and two simulated frame flange's consisting of a 12-ply layup of [45/02/-45/04/-45/02/45]. Test surface finished with one layer of copper mesh and one layer of glass fibre.

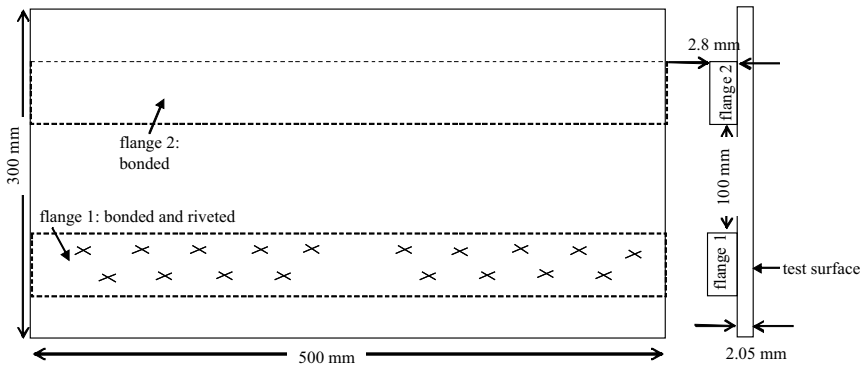

Figure 8: *Diagram of the skin-frame flange panel showing flange 1 as the bonded and riveted frame and flange 2 as the bonded frame.*

3.3 Vaseline contamination

Two C/Ep composite panels were fabricated by Hawker de Havilland and supplied for inspection by the CRC-ACS. Both panels consisted of a 12-ply monolithic laminate panel and two simulated frame flanges, one bonded to the skin panel and the other bonded and riveted in place (Figure 8). Table 3 shows the layup of the specimens. Specimen 2 differed in that the inspection surface was finished with a single layer of copper mesh beneath a single glass fibre layer. The panels incorporate vaseline inclusions to simulate disbonds, as well as impact damage of varying severity (impact energy levels) including barely visible impact damage (BVID). Information about the defect types and positions were supplied by the CRC-ACS after the testing was completed.

Sonic thermography was conducted with a nominal input power of 480 W over 1 second duration. The thermal data was acquired at a frame rate of 50 Hz over 750 frames giving a total inspection time of 15 s. Figures 9(a) and 10(a) show the damage maps of specimens 1 and 2, respectively, which combine the known location of the vaseline inserts and point of impact positions with the result of a C-scan of the specimen, which revealed the true extent of the impact damage. The circular areas correspond to vaseline inclusions, the red crosses are the impacted sites and the larger red outlines indicate the regions of damage as disclosed by the C-scans. The ST result obtained for specimen 1, superimposed with a photograph, is shown in Figure 9(b). The detected defect regions are highlighted by the

boxes. Insonification was applied to the central left of the specimen. The impact damage caused by I1, I4, I5 and I6 was detected. Frictional and/or anelastic heating occurs around the edges of the impacts as shown by the outline of the impact damaged regions of I4 and I5. This also suggests that the impact damage has caused large air gaps, and this is confirmed by the FT results (Figure 9(c)), which indicate a larger thermal resistance within the outlined region. The strong localised thermal signature at the bottom right of the impact damage and region corresponding to I4 and I5 coincides with the position of one of the vaseline inclusions. Indications of impacts I2 and I3 and the centrally positioned vaseline inclusion in the lower flange (flange 1), located at the centre of the fastener region (highlighted by the box) are also evident in the ST result. It should be noted that these indications also exhibit a periodic modal signature which contributes some uncertainty to the identification of these as defects. The reason that the other vaseline inclusions were not detected may lie in the fact that, like Teflon, vaseline may hinder the production of frictional heating during insonification. Thermal indications were also observed along the upper edge of the riveted flange panel, indicating frictional heating between the flange and the skin. Also, indicated by the arrow, are vibrational mode patterns due to anelastic heating.

In Figure 10(b) the ST result for specimen 2 indicates significant damage in the I6 impact region. The insonification was applied to the central right of this specimen. The thermal signatures correspond to the edge of the damage area, which is, evidently, in compression. Faint indications of the impact damage caused by I2, I3 and I5 were detected, however these are difficult to distinguish from the modal vibration patterns (indicated by the arrows). In a blind test it would be difficult to conclusively determine that these areas corresponded to damage. None of the vaseline inclusions were detected, partly for the reason stated previously, and also because the detection of defects is hindered by the Cu mesh/ fibreglass finish, which acts to diffuse heat in the lateral or in-plane direction. The extra plies also increase the diffusion length, resulting in a reduction in the thermal signature. FT was unable to detect any damage or inclusions (Figure 10(b)).

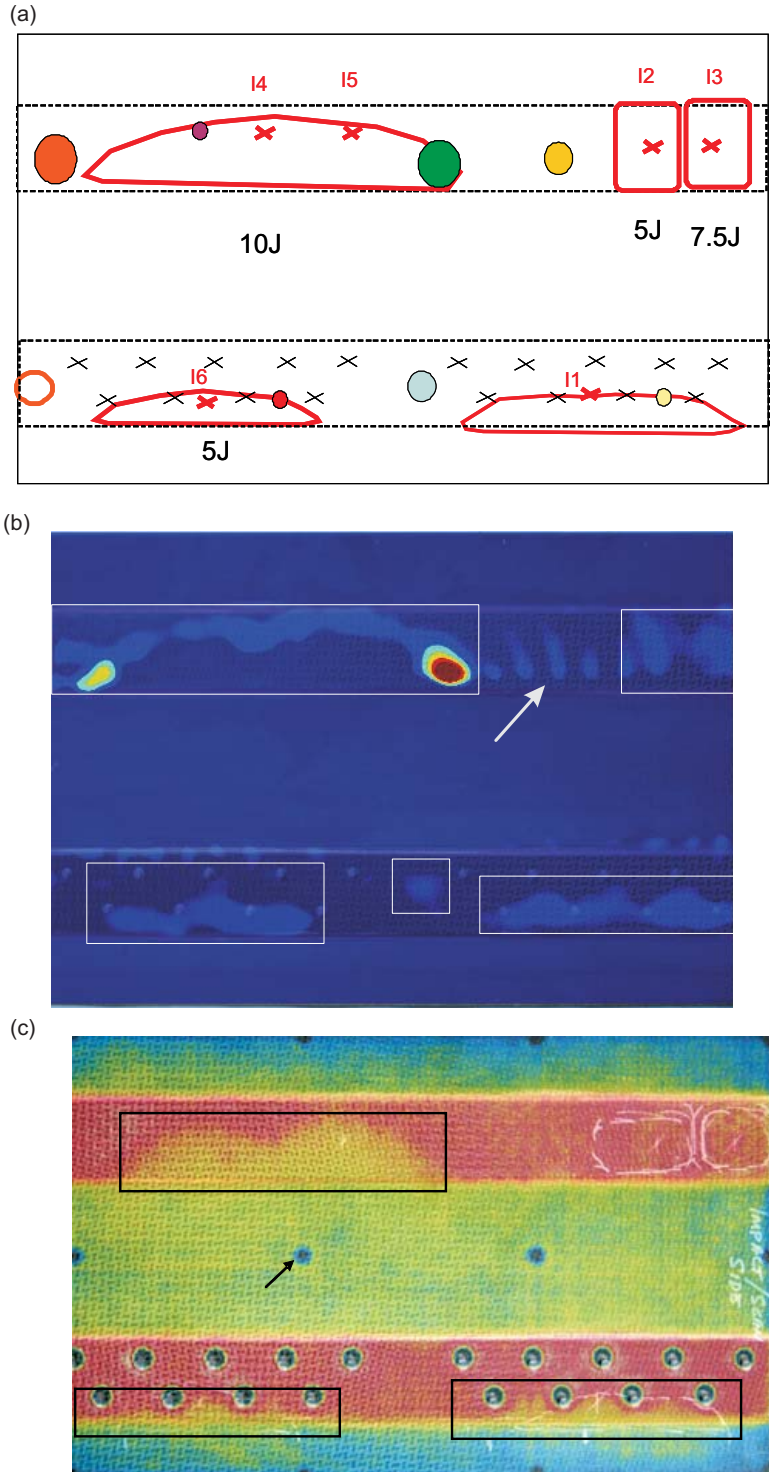

Figure 9: *(a) Damage map, (b) ST result (PCT_3) and (c) FT result of specimen 1. The results shown in (b) and (c) are of the respective thermographs which have been superimposed with a photograph of the panel. In (a) the coloured circles correspond to the vaseline contamination in the bondline, red crosses indicate impact fractures and areas marked by the red outline indicate damage disclosed by C-scans. In (b) the arrow indicates vibrational mode patterns due to anelastic heating. Note that the blue circles in (c) (an example of which is indicated by the arrow) are markers used for alignment of the thermographic images.*

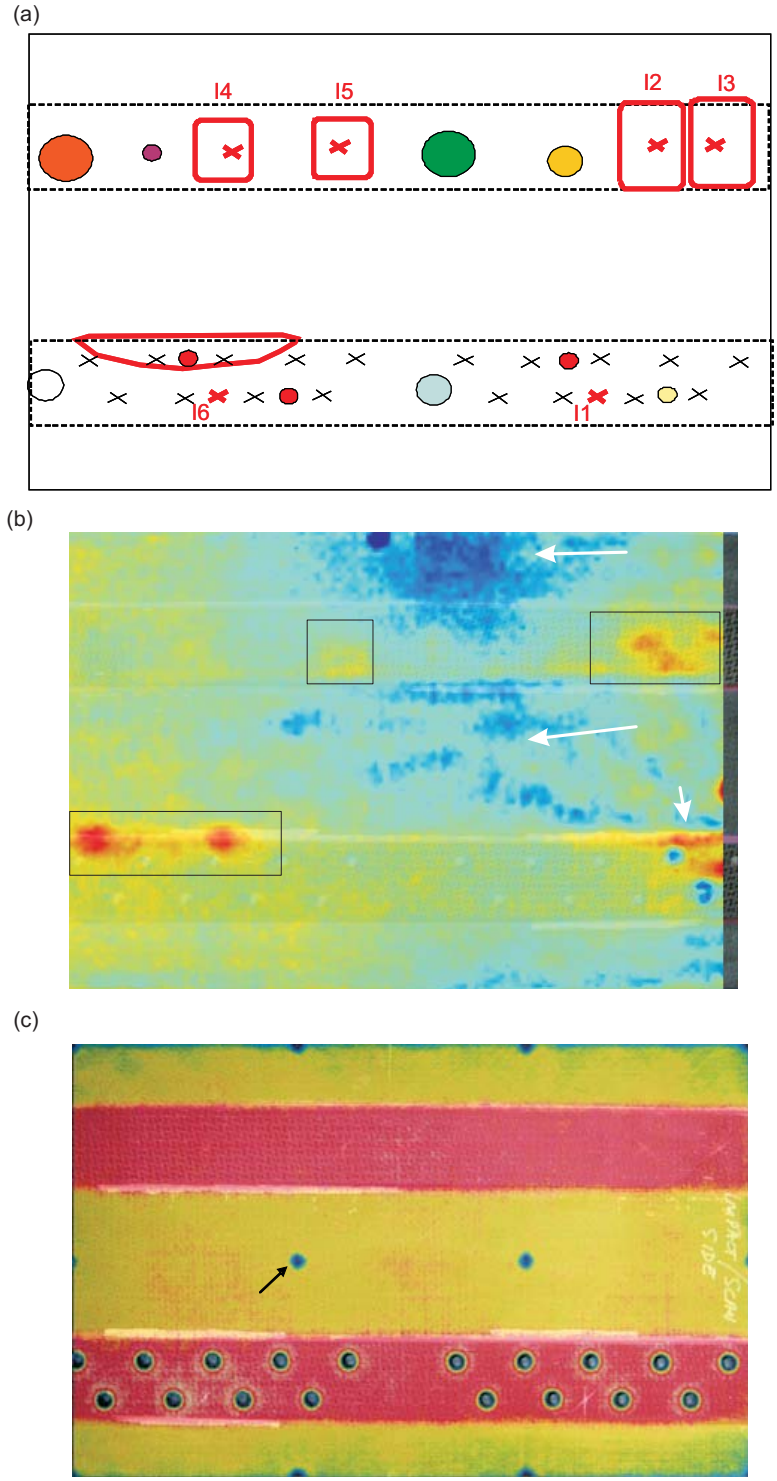

Figure 10: *(a) Damage map, (b) ST result (phase) and (c) FT result for specimen 2. The results shown in (b) and (c) are of the respective thermographs which have been superimposed with a photograph of the panel. In (a) the coloured circles correspond to the vaseline contamination in the bondline, red crosses indicate impact fractures and areas marked by the red outline indicate damage disclosed by C-scans. In (b) the arrows indicate vibrational mode patterns due to anelastic heating. Note that the blue circles in (c) (an example of which is indicated by the arrow) are markers used for alignment of the thermographic images.*

3.4 Glass reinforced aluminium specimens

A series of glass reinforced aluminium specimens were being used in an investigation by researchers at Monash University to study the efficacy of computed tomography as a means of detecting disbonds [15]. These fibre reinforced metal laminates (FML) are of great interest to the aerospace industry primarily due to the superior strength to weight ratio as compared to a monolithic metallic structure. Thermography was used as a comparative NDE technique. The specimens consisted of two aluminium 5005 plates, of dimension 400 mm x 400 mm x 1.5 mm, bonded together with a layer of woven E-glass-fibre reinforced epoxy approximately 1 mm thick. Teflon inserts of diameter 40 mm, 80 mm and 100 mm were embedded in the lower half of the plate, between the aluminium and the E-glass-fibre layers during fabrication in order to simulate disbonds. Inspections were made with the inserts positioned below the E-glass-fibre. FT was unsuccessful at locating the inserts.

FML are a potentially difficult candidate for any thermographic technique because of the presence of the metallic skin. This skin facilitates lateral diffusion of thermal signals that emerge from the polymer interior. Because these signals are invariably quite weak, especially if produced through flash inspection, the strong lateral heat diffusion in the metallic skin can hinder detection of internal flaws.

ST was completed, using a 5 s insonification time, with the acoustic horn set to 500 W. The thermal image was captured at a 15 Hz frame rate for 300 frames. The PPT and PCT_2 results are shown in Figure 11. The inserts were easily located. Figure 12 shows sonic thermographs which were taken for the same plate with the inserts positioned below the E-glass fibre ((a) and (b)) and then an inspection was made of the opposite side of the plate with the inserts positioned above the E-glass fibre ((c) and (d)). From Figures 12(c) and (d) it can be seen that when the inserts are positioned above the E-glass fibre the thermographic indications are more distinct, as is to be expected.

3.5 Lapjoint specimen

Accepted practice in composite patch design is to taper the edge of the patch [16]. In an attempt to optimise taper geometry an experimental study was conducted on various patch geometries, in which specimens were exposed to mechanical loading and non-destructive testing was applied to inspect for damage in the taper region. The specimens were made of 2024 aluminium alloy with the dimensions 220 mm x 20 mm x 6.2 mm. The patches consisted of ten plies of boron fibre epoxy (B/Ep) laminate with one layer of FM73 adhesive, co-cured to the bottom surface of the patch. The patches were applied to both sides of the aluminium alloy blanks. Under constant cyclic loading disbonding of the patch can occur and ST inspection was conducted on one such specimen.

Figure 13 shows photographs of sides A and B of the lapjoint and the corresponding PPT results for each side during insonification. The PPT results for both sides clearly show a bright vertical band mid way through the patch. This corresponds to where the specimen was gripped in the tensile machine and is likely to indicate localised sub-surface damage caused by the grips. On the far right of both thermographs there is an indication of a strong heat source corresponding to the disbonded patch edge. Heat production occurs due to frictional heating between the disbonded patch and the aluminium face. There are

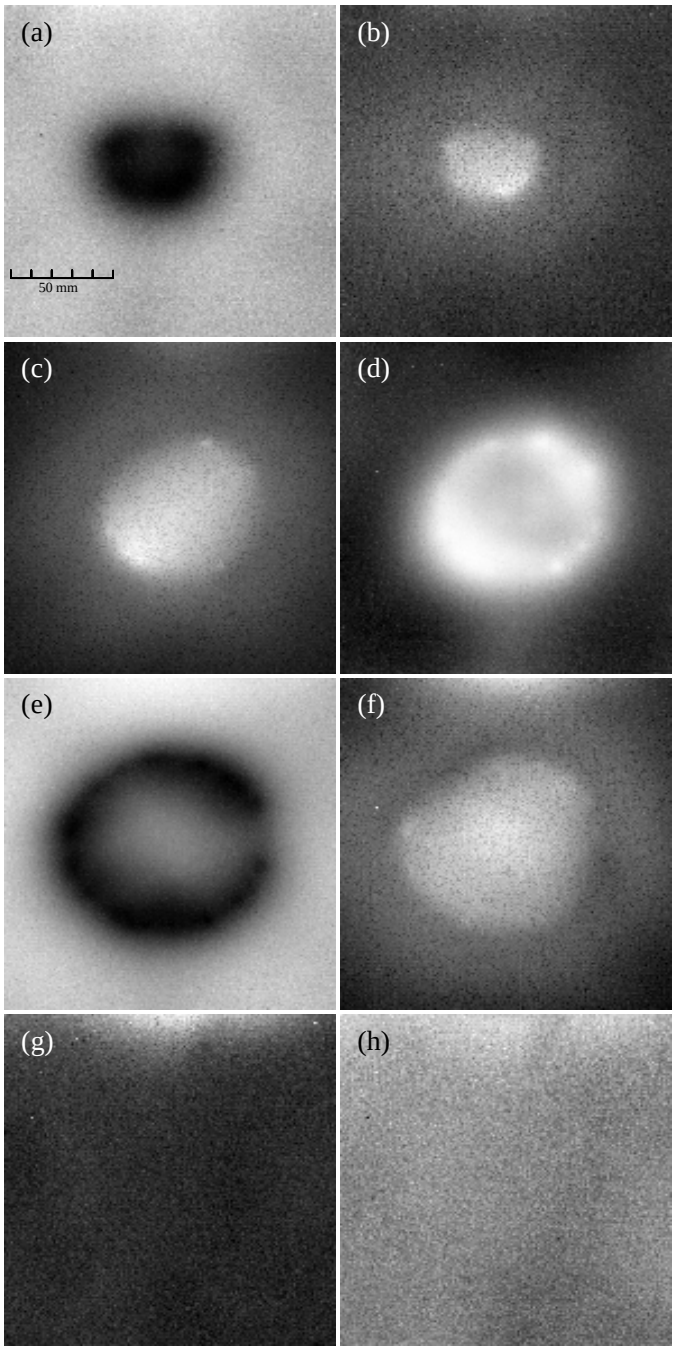

Figure 11: *Sonic PPT (left) and PCT_2 (right) results of glass reinforced aluminium specimens with embedded Teflon inserts with varying diameters of (a-b) 40, (c-d) 80 and (e-f) 100 mm respectively. (g-h) correspond to a reference specimen.*

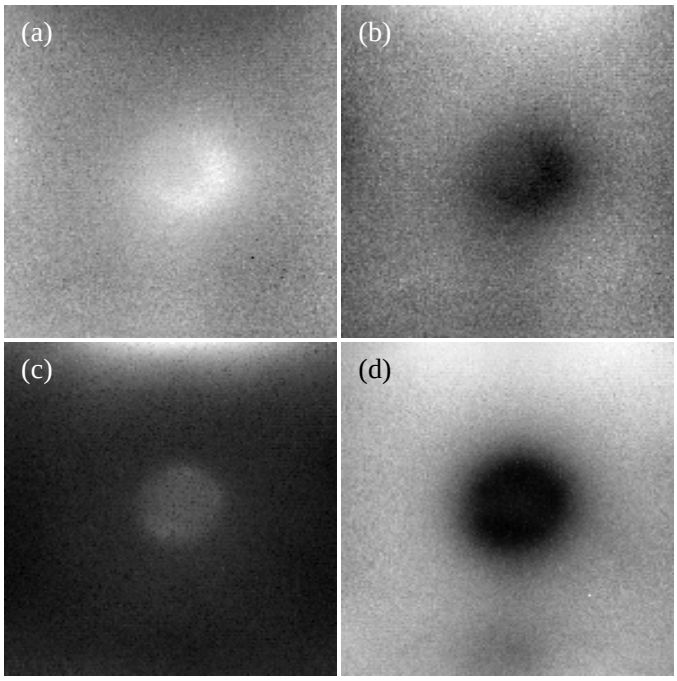

Figure 12: *PPT (left) and PCT_2 (right) results of glass reinforced aluminium specimens with embedded Teflon inserts captured with the inserts below the E-glass-fibre (a-b) and above the E-glass-fibre (c-d).*

also indications at the corners of the patch, on the far left of the thermographs, which points to further damage due to the gripping of the specimen in the mechanical testing machine.

3.6 F-111C: A15-5 lower wing skin section

Two fragments (12W951A1 and 12W951X) of a composite reinforced section of an F-111C (A15-5) lower wing skin (LWS) were inspected using both ST and FT. These fragments were sourced from a wing section that had failed during a full-scale fatigue test reported elsewhere [17], providing an opportunity to evaluate a range of NDE techniques on a real repair. The presence of a B/Ep doubler is known to pose serious challenges for conventional ultrasonic inspection, to the extent that tap testing is often the preferred method of inspection where disbonding of a B/Ep reinforcement was suspected [18]. Given this, the case is especially useful in highlighting the relative performance of thermographic techniques on a known difficult inspection problem.

Figure 14 shows the experimental setup for the LWS fragments. The LWS fragments were insonified for 10 s, with the acoustic horn set to 500 W, and a foam interface was used between the acoustic horn and the specimen. Thermal image capture was conducted with a frame rate of 10 Hz, and 300 frames were recorded. Figure 15 shows (a) a photograph of the LWS fragment 12W951A1, the area of interest is circled, and (b) the corresponding raw ST result. Regions A and B clearly show zones of elevated heat production (dark areas) which indicate a disbond or delamination. Interestingly, the heat production is noticeably

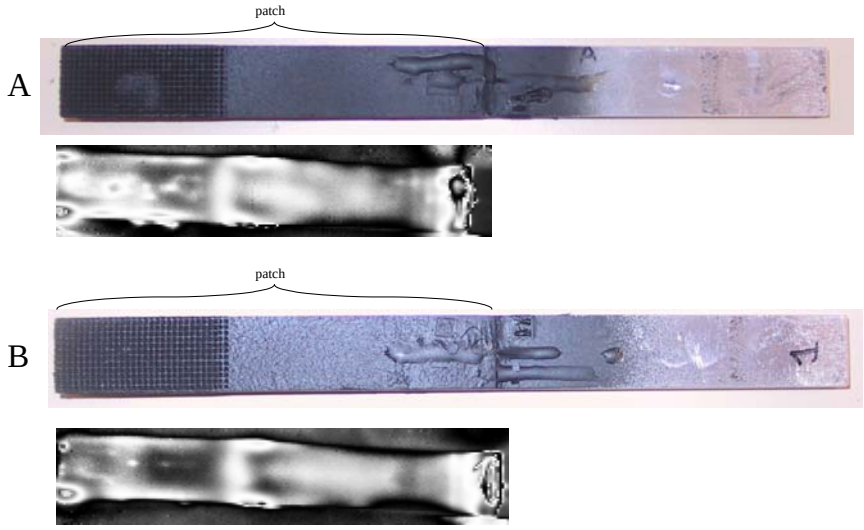

Figure 13: *From top to bottom, photograph of lapjoint side A, corresponding PPT result, photograph of lapjoint side B and its corresponding PPT result.*

uneven across the defect suggesting either a non-uniform distribution of contact stress and hence frictional force acting across the defect surfaces or the presence of a 'local' resonance induced by the acoustic excitation. Region C shows anelastic heating caused by a vibrational mode in the structure. The raw ST data was further examined using PPT and PCT methodologies. Figure 16 shows the (a) PPT and (b) PCT results for the region of interest taken from the ST inspection. The image furnished by PCT tends to show more detail within the disbond region, whereas PPT produces clearer images of the modal resonances within the structure. The results, shown in Figure 16, highlight the presence of additional spatial detail, not evident in the raw data. Figure 17 shows a comparison of the ST results with FT and a C-scan. Whilst the defects are evident in both the FT and the C-scan, the contrast furnished by ST is markedly superior and the size of the indication is noticeably larger than that shown in the FT result, suggesting that some part of the disbond is under a compressive load (kissing bond).

A photograph of the other LWS fragment, 12W951X, is shown in Figure 18 and Figure 19 shows the PCT results (a, b, d and e) and corresponding flash thermographs (c and f) for regions D and E, as indicated. It is noted that a non-grey colour map is used in this case merely to accentuate indications, and does not indicate relative temperature; that is whether a region is hotter or colder. The PCT results show clear indications of disbonding (circled) which are not as strong in the FT results (c and f). Once again the spatial detail is superior in the ST results.

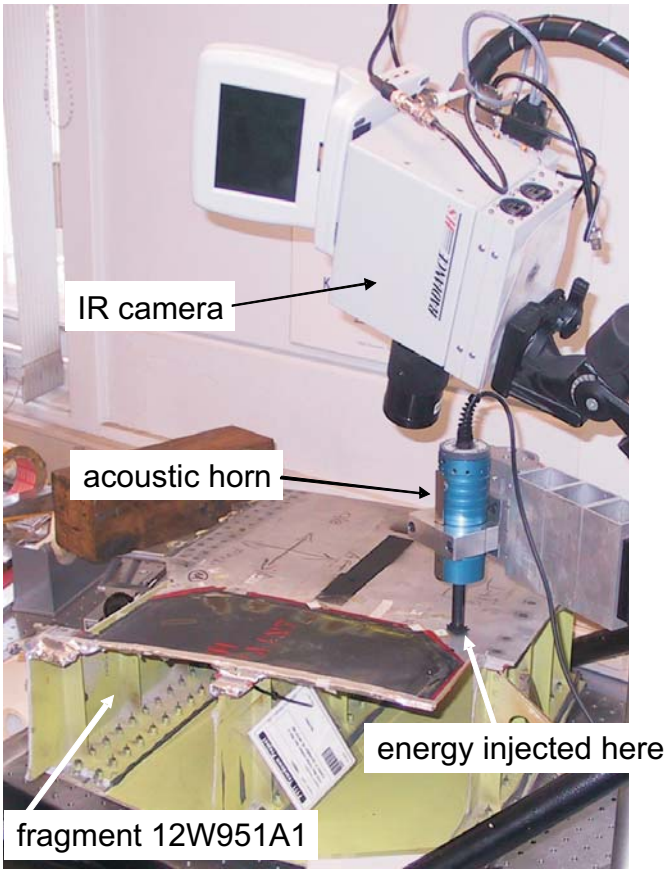

Figure 14: *Photograph of the experimental setup showing the specimen, acoustic horn and thermal camera.*

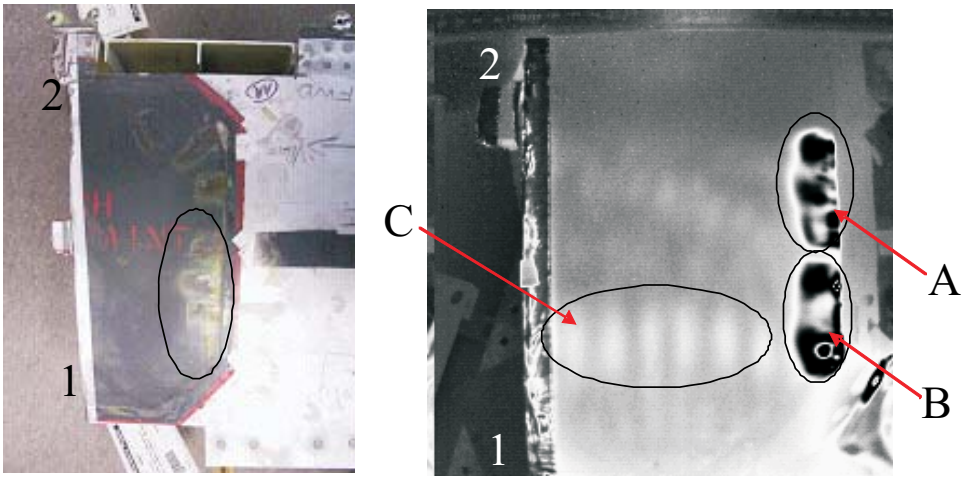

Figure 15: *(a)Photograph of the LWS fragment 12W951A1 indicating region of interest. (b) Raw ST image showing darkened regions indicating elevated heat production and possible disbonds.*

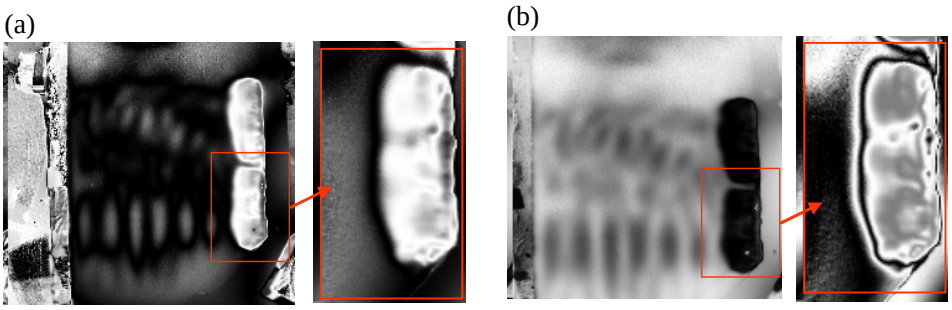

Figure 16: *(a) PPT and (b) PCT results elucidating the disbond in regions A and B. Different grey scales were used in order to accentuate the flaw regions.*

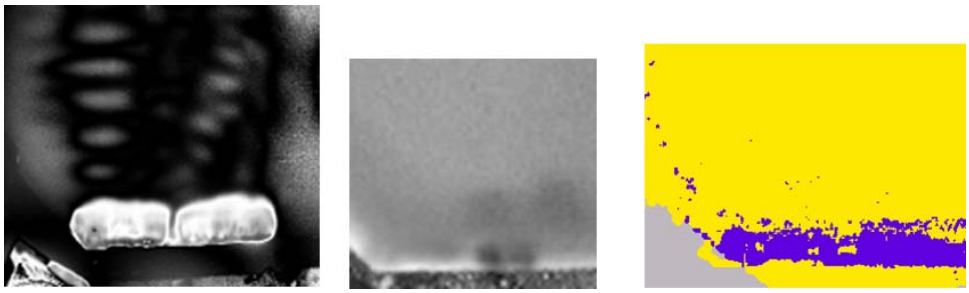

Figure 17: *Comparison of sonic PPT, flash PPT and C-scan results, respectively showing the disbonds in regions A and B.*

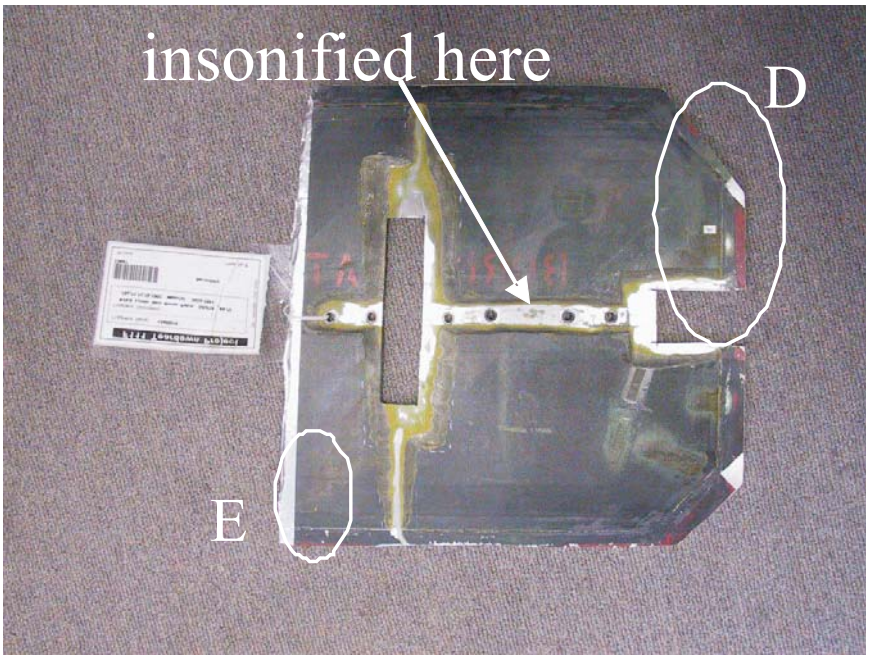

Figure 18: *Photograph of fragment 12W951X, indicating regions of interest, D and E and point of insonification.*

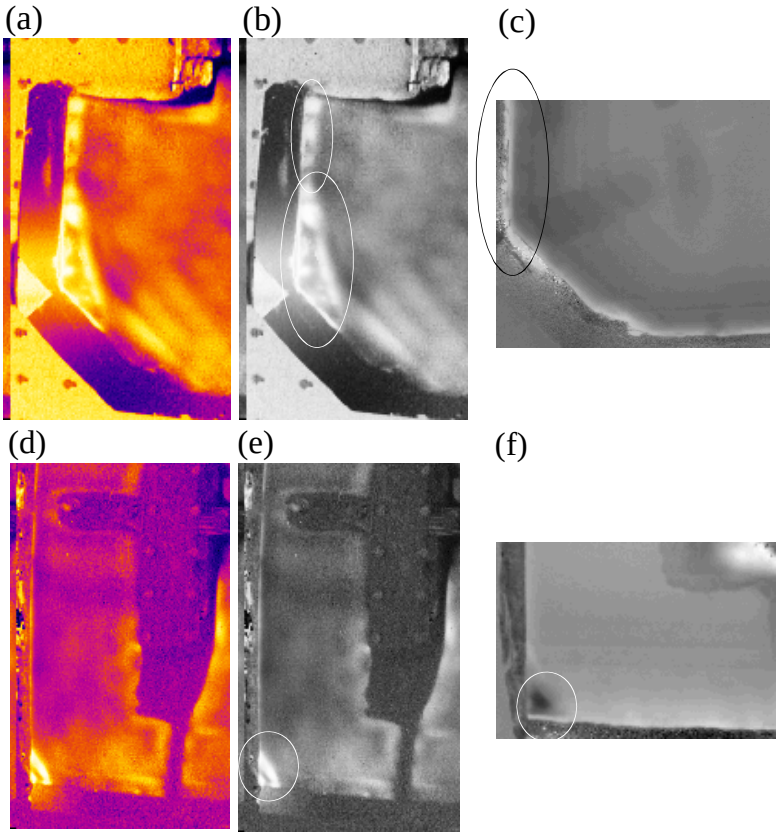

Figure 19: *(a) and (b) are the sonic PCT_2 results of region D and (c) the corresponding flash PPT result of the same region (circled) and (d) and (e) are the sonic PCT_2 results of region E and (f) the corresponding flash PPT result.*

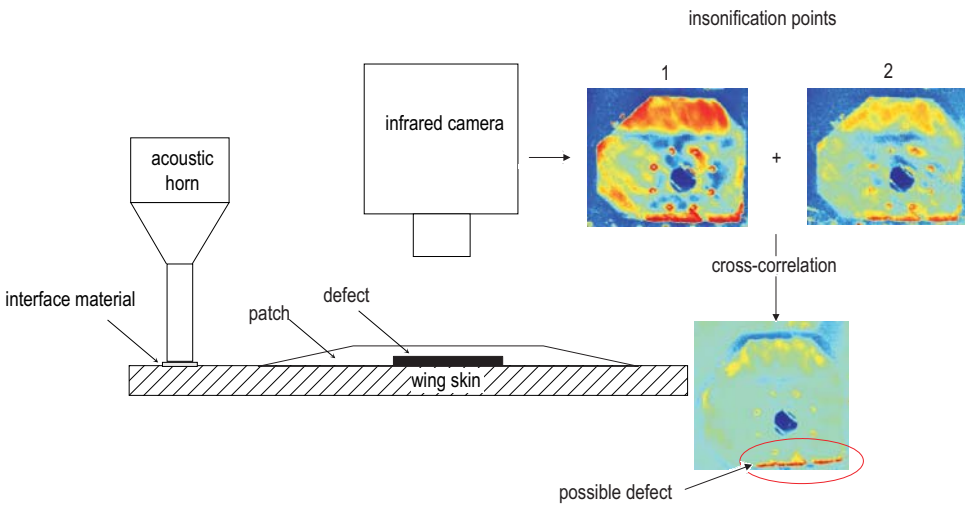

Figure 20: *Diagram of the experimental setup used for ST of the Mirage III boron patches.*

3.7 Mirage III Boron Patch Teardown

When the Mirage III aircraft was in service with the ADF, one of its known structural deficiencies was a susceptibility to fatigue cracking in the lower wing skin. In order to retard crack growth the area was reinforced with a B/Ep composite patch. The patch consisted of 7 internally stepped plies of an adhesively bonded, unidirectional B/Ep reinforced laminate. The patches were adhered to the wing skin structure using a modified film epoxy adhesive (AF-126 by 3M). In October 2001, seventeen B/Ep composite patches were removed from the lower wing skin section of Mirage III aircraft that had been in storage in Woomera since 1989. The patches underwent NDE [2] using ST, FT, tap testing and BaNDIcoot [20]. Adhesion tests were then conducted on areas of the patch which showed an indication of degradation by the NDI. The patch was then removed for closer inspection.

Figure 20 shows the experimental setup for the ST of the Mirage III patches under investigation. For each patch a minimum of 2 insonification points were used. Each insonification excites a vibrational mode shape, which can mask the defect information. By performing a cross-correlation between the separate results, the effect of modal artefacts are reduced, and the defect information accentuated. The patch was insonified for 2 s using a felt interface. The acoustic horn was set at 500 W and a total of 300 frames were captured at a frame rate of 20 Hz. The results were processed using PCT.

Figure 21 shows a photograph of a typical Mirage patch under investigation. Figures 22(a) and (b) show the flash PPT and sonic PCT_2 results of the patch, respectively. Figures 22 (c) and (d) show the results obtained using the bandicoot system, in which the peak defect index was set to 4% at 9-15 kHz in (c) and 2% at 25-35 kHz in (d). The indicated areas in Figure 22(b) show regions of elevated heat generation corresponding to possible defects. While the FT scan does contain some contrast in the regions shown by ST to be flawed, the indications are quite diffuse and difficult to interpret. The BaNDIcoot system

[2]Tap testing, BaNDIcoot and the pull out test results shown in this section were obtained via private communication with Andrew Rider [19]

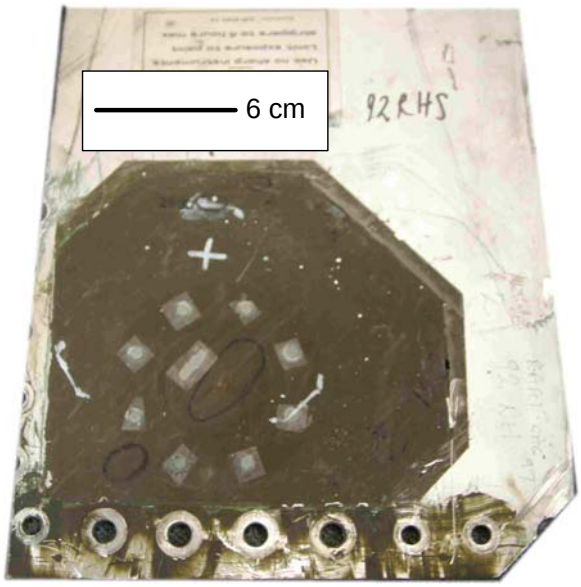

Figure 21: *Photograph of a typical Mirage III boron patch under investigation.*

revealed several suspect sites in areas broadly consistent with the ST result, however the scan indicates a more localised distribution of damage than that suggested by ST.

Having completed the NDE survey, the Mirage III boron patches were then destructively tested using an adhesion tester. A pullout stub of 12.7 mm diameter was adhered to a cutout of the wing skin, of similar dimension. This saw cut is extended through the wing skin to the adhesive layer. The pullout stub was attached to the skin using adhesive EA9309.3NA. The pullout stub was then attached to a piston device which measures the residual strength of the adhesive bond. The results of the pullout tests showed that ST produced the highest predictive accuracy for areas of low strength within the bondline. Table 4 shows the comparative results of the pull out tests on the seventeen patches for the ST, tap testing and BaNDIcoot. A pull-off tensile strength (POTS) below 750 psi was assumed to correspond to bondline degradation [19] and the number of indications with a POTS <750 psi are shown in the third column. A large value in this column correlates to improved detection of bondline degradation. However this increase in sensitivity can be detrimental in that there may be a higher rate of false positives, as observed with the BaNDIcoot system which had a total of 76 indications with 39 of those relating to degradation. For ST, 52 indications corresponded to the pull off stub test areas and of these 36 were consistent with bondline degradation. It should also be noted that indications furnished by ST were often of a size smaller than the diameter of the pullout stubs (indicated in Figure 22(b)), which suggests that ST may be more sensitive to these weak bond areas. This is an important result as it indicates that ST may in fact be more sensitive to weak bonds than the results listed in Table 4 suggests. Further investigation is required in order to obtain a more accurate and quantitative assessment of the ability of ST to detect degraded or weak bonding in patched systems.

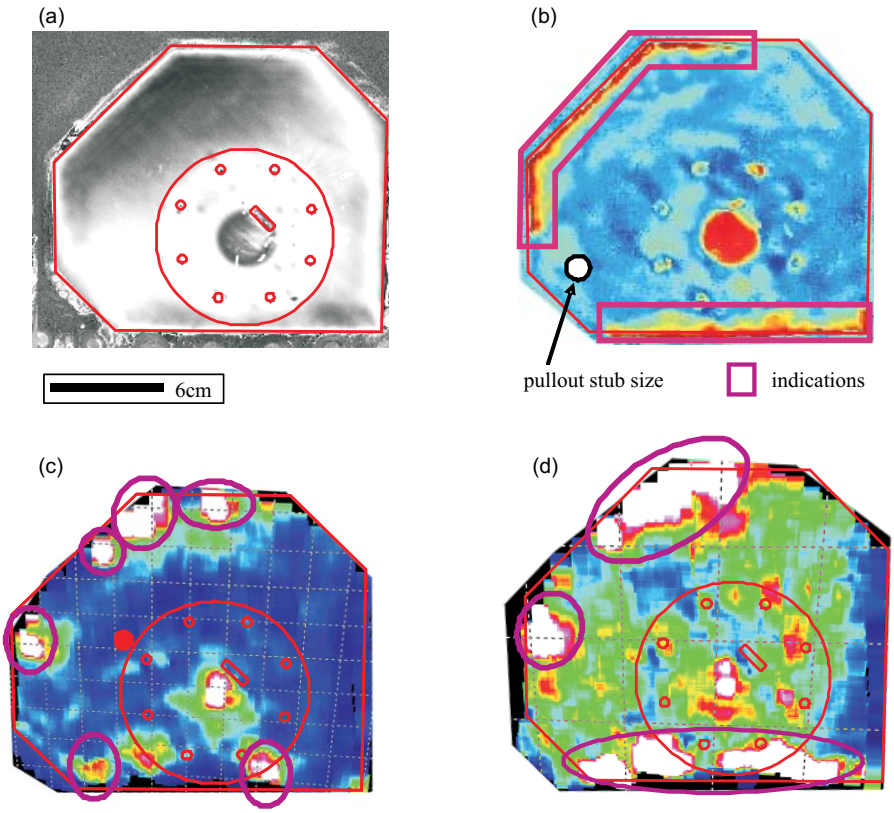

Figure 22: *Results for (a) flash PPT (b) sonic PCT_2 (c) BaNDIcoot with peak index set at 4% and 9-15 kHz and (d)BaNDIcoot with peak index set at 2% and 25-35 kHz. The defect indications are circled in pink. An example of the pullout stub size is shown in (b) as a white circle.*

4 Impact damage detection

Impact damage to composite structures, especially BVID, often leaves no noticeable surface indication, yet can cause profound subsurface damage. Accordingly, it is an important class of nondestructive inspection problem.

4.1 Impact damage in carbon fibre composites

Galea and Chiu [21] reported on a study on the effect of multiple BVID on the residual compressive strength of composites in which a series of composite specimens were impacted. The specimens were 6.7 mm thick laminates comprising 50 plies of an AS4-3501 C/Ep system in the layup sequence: $[+45_2/-45_2/0_4/+45_2/-45_2/0_4/+45_2/-45_2/0_4/90]s$. The specimens had been retained by the authors and were made available for inspection by ST. The first specimen had two impacts, each with 8 J of incident energy. Figure 23(a) shows an image of the impact sites. From the photograph, the impact on the right shows major damage due to compressive loading which was carried out after the impacts were made. From a simple visual inspection the impact on the left is difficult to observe. Both sites are circled. The specimen was insonified for 5 s with the acoustic horn set to 500 W

Table 4: *Comparison of the accuracy of NDI indications.*

Technique	Indications	
	total	< 750 psi
ST	52	36
Tap Testing	39	26
BaNDIcoot	76	39

with 300 frames captured at a frequency of 10 Hz. Figures 23(b) and (c) show the raw thermal image and the PPT result, respectively. From the raw thermal image the impact region on the left is not observable though both the sonic PPT (c) and PCT_2 (d) results reveal the defect clearly. Figure 23(e) is the flash PPT result of the same region and the defect is clearly seen.

The second C/Ep specimen had a single BVID also with 8 J initial impact energy. The specimen was also insonified for 5 s with the acoustic horn set to 500 W with 300 frames captured at a frequency of 10 Hz. Figure 24 shows the specimen with the impact region marked by the square. Figure 25 shows the (a) sonic PPT, (b) sonic PCT_3 and (c) flash PPT results. Normally, processing the raw thermographic data would eliminate most emissivity related features, however in this case, the ink markings on the specimens are still apparent in the FT result, though this has had a negligible impact on the detectability of the flaw.

4.2 Step lapjoint specimen

A step lapjoint was manufactured [22] in order to study the effect of BVID on the structural integrity of metal to composite joints. The 'final wing root joint' coupon investigated is detailed in Van Blaricum [22]. It consisted of AS4/3501-6 C/Ep laminate bonded to 6A1 - 4V titanium using FM300K adhesive. After being impacted on both sides with a 12 mm diameter spherically tipped impactor, the specimen was loaded under compression in a 500 kN servo-hydraulic test machine in order to determine whether the specimen would undergo delamination failure. The specimen was insonified for 5 s, the acoustic horn set to 500 W, and a frame rate of 10 Hz over 300 frames was used. Figure 26 shows the specimen; the impact region is at the centrepoint of the white cross and the region of interest is outlined by the square. The sonic PCT_2 (left image) and FT PPT (right image) results are also shown. Both results show that the damage is slightly off centre, located below and to the left of the impact.

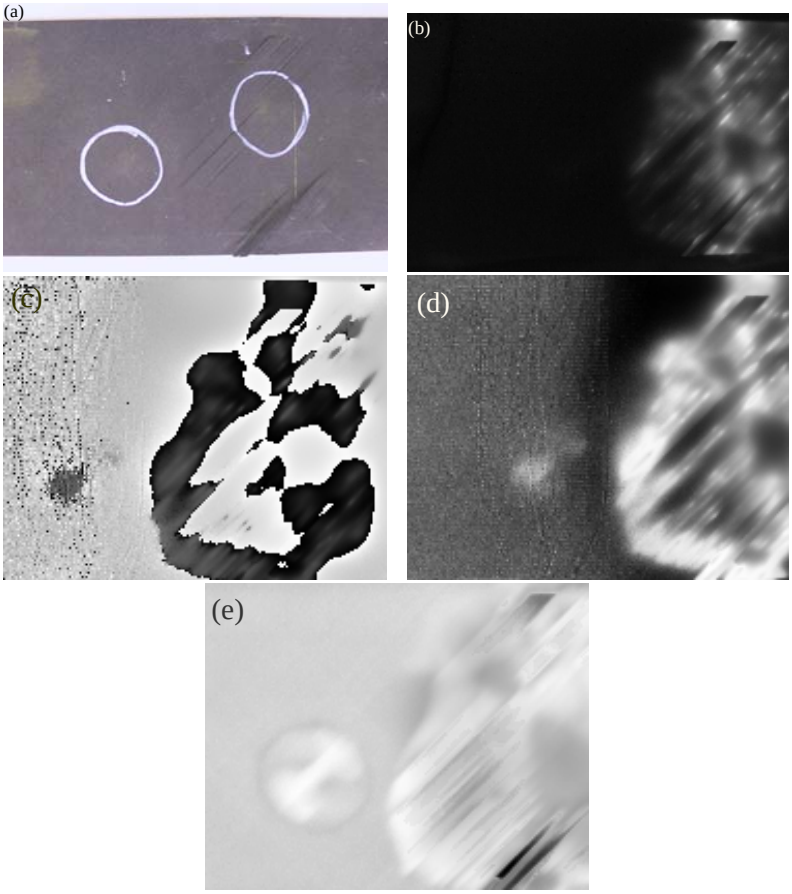

Figure 23: *(a)Photograph of the impact damaged regions of the composite specimen; impact regions are indicated by the circles. ST (b) raw, (c) PPT and (d) PCT_2 results and (e) flash PPT result of the impact damaged regions of the composite specimen.*

Figure 24: *Photograph of the single impact specimen with the impact region indicated by the square.*

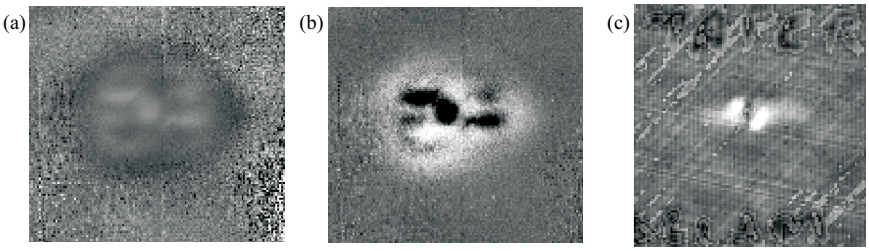

Figure 25: *The ST (a) PPT and (b) PCT_3 results and the (c) flash PPT result of the impact damaged region of the composite specimen.*

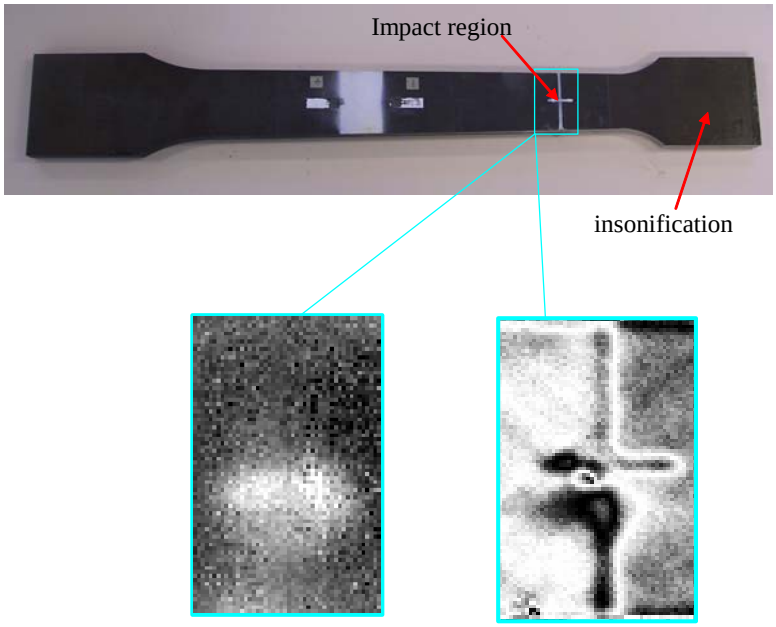

Figure 26: *Photograph of the step lapjoint specimen showing the impact region and the insonification point. The bottom left image is the sonic PCT_2 result and the bottom right image is a flash PPT result of the damaged region.*

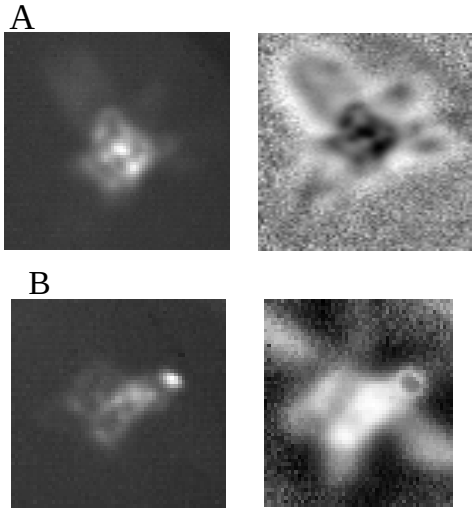

Figure 27: *Raw ST (left) and PCT_2 (right) results, respectively, for Syncore specimens A and B.*

4.3 Syncore specimens

Impact damaged specimens made with 'Syncore', a registered trademark of Loctite aerospace, were investigated. Syncore is a toughened, low density epoxy syntactic core material, of foam-like appearance, that is designed to be sandwiched between composite face skins to create a structural panel with a high strength to weight ratio. One of the main concerns with this advanced material is its questionable impact resistance. In a preliminary study on its impact resistance several specimens were manufactured, exposed to a controlled impact and then non-destructively inspected. Two samples were made available for thermographic inspection. In preliminary testing it was found that only a relatively short insonification (< 0.5 s) was required to produce a strong indication of damage. The unprocessed and PCT_2 results are shown in Figure 27 for the two samples. The results show that even an unprocessed thermograph renders a strong indication of subsurface damage. The panel appears to be an ideal candidate for thermographic inspection as the core seems to suffer profound damage under impact, leading to a large thermal signature, while the thin composite skin presents little obstruction to the transfer of heat from the core to the specimen surface.

Table 5: *Table showing the layup of the received specimens (courtesy CRC-ACS).*

Specimen 1A	9 plies with layup of [45/0/-45/90/0/90/-45/0/45]
Specimen 1B	9 plies with layup of [45/0/-45/90/0/90/-45/0/45] with a fibreglass and copper mesh finish (specimen is curved)
Specimen 2A	Honeycomb sandwich panel consisting of 9 plies in the stabiliser skin with a layup of [0/0/0] and 9 plies for the stress skin with a layup of [45/0/-45/-45/0/45]
Specimen 2B	Honeycomb sandwich panel consisting of 9 plies in the stabiliser skin with a layup of [0/0/0] and 9 plies for the stress skin with a layup of [45/0/-45/-45/0/45] with a fibreglass and copper mesh finish

Table 6: *Table showing the energies used in the impacts on specimens 1A, 1B, 2A and 2B (courtesy CRC-ACS).*

Impact site	Impact energy (J)	Impact site	Impact energy (J)
IP1	12.5	IU1	7.5
IP2	7.5	IU2	12.5
IP3	5	IU3	10
IP4	10	IU4	5
IP5	15	IU5	15

Note: IP5 and IU5 impacts are only applicable to specimen 2B.

4.4 Detection of impact damage and artificial inclusions in composite panels.

A series of four C/Ep composite panels, representative of MRH-90 composite structure, were fabricated by Hawker de Havilland. Table 5 indicates the layup of the specimens. The panels contained Teflon inclusions, to simulate disbonds, as well as impact damage at several different energy levels (Table 6), including BVID. The specimens had a primer and paint layer applied to one half of the inspection surface to determine what effect this would have on the detectability of the defects. Preliminary inspections confirmed no significant differences between unpainted and painted surfaces. The upper half of the specimens contained impact damage and the lower half contained various sized Teflon inserts. Information about the defect types and positions were supplied by the CRC-ACS after the testing was completed. Specimens 1B and 2B had a copper mesh embedded just below the inspection surface (see Figures 29 and 32). The entire inspection surface for each of the panels was coated with a high emissivity paint prior to inspection.

Figure 28 shows the ST and FT results for specimen 1A and the corresponding damage

map. The detected damage is highlighted by the red arrows. DP1, DP4, DP5 and DP9 show very faint thermal indications and DP6 shows a clear indication in comparison to the FT of the same defect. This may indicate higher contact stress of the faces of this defect compared to others. The circled regions, at the top right and bottom left of the thermograph, show thermal indications from lead targets situated on the back of the specimen. Based on the rule of thumb described in section 3.2 and the known skin thickness given the diffusion length, all disbond defects should have been observable. None of the 5 mm diameter inclusions and some of the 12.5 mm inclusions were detected using ST, whilst all but DP3, DU6 and DU9 were detected using FT. As a general rule a Teflon insert is a poor approximation to a disbond for a ST procedure since the coefficient of friction is low between the Teflon and the laminate, thus producing a lower amount of heating than would be expected for a real disbond. A closer examination of the ST images of the inclusions that were detected reveals a ring like appearance, similar to that observed for impact damage. This suggests that anelastic heating of the composite due to higher strains at the edges of the inclusions may be contributing significantly to the thermal signature observed.

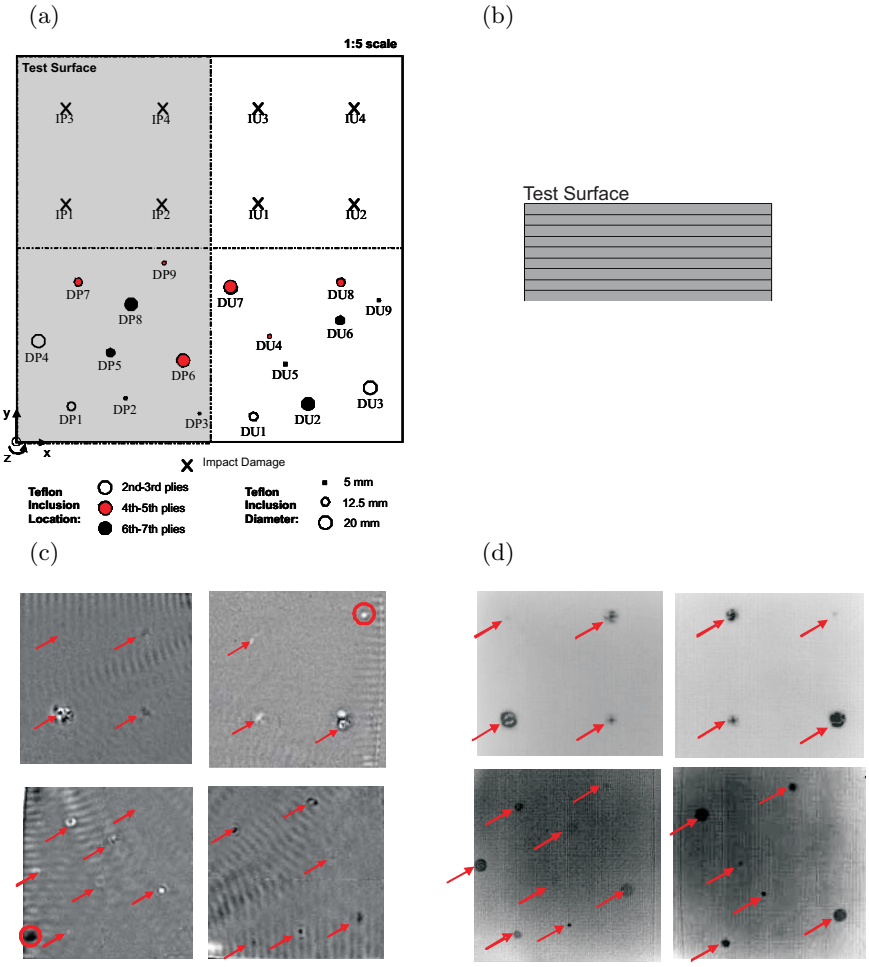

Figure 28: *(a) Damage map, (b) profile image of layup, (c) sonic and (d) flash thermographs showing the four quadrants of specimen 1A and the corresponding damage locations. The 'U' and 'P' refer to the damage locations on the unpainted and painted side of the specimen, respectively. (Specimen layout courtesy CRC-ACS.)*

Figure 29 shows the ST and FT results for specimen 1B and the corresponding damage map. The presence of the glass fibre/ copper mesh layers significantly reduces the effectiveness of both ST and FT. This can be attributed to a number of factors. Specimen 1B is 3 plies thicker than specimen 1A, thus increasing the defect depth, resulting in a fainter signature. Also, if only the edges of the inclusions are contributing to the heating, as was speculated for specimen 1A, the area of the defect which contributes to heating is smaller than the defect itself, reducing its detectability. The existence of the copper mesh layer also has a deleterious effect by increasing the amount of lateral diffusion. The effect of the copper mesh on the thermal signature can be observed in the impact damage signatures of the two specimens (with and without mesh). The sonic thermographs of the impact damage in specimen 1A shows distinct detail, particularly for the high energy impacts (12.5 J) of IP1 and IU2. In comparison, the equivalent impacts in specimen 1B are detected, however the signatures appear smeared, and lack the detail seen for specimen 1A.

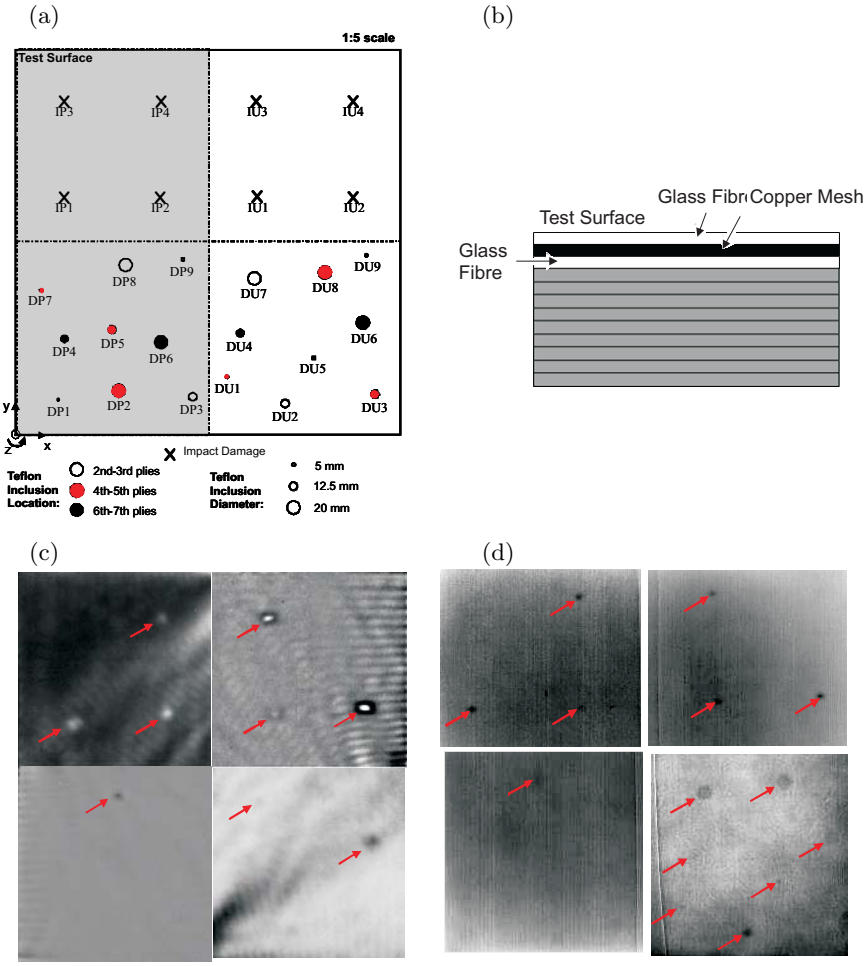

Figure 29: *(a) Damage map, (b) profile image of layup, (c) sonic and (d) flash thermographs showing the four quadrants of specimen 1B and the corresponding damage locations. (Specimen layout courtesy CRC-ACS.)*

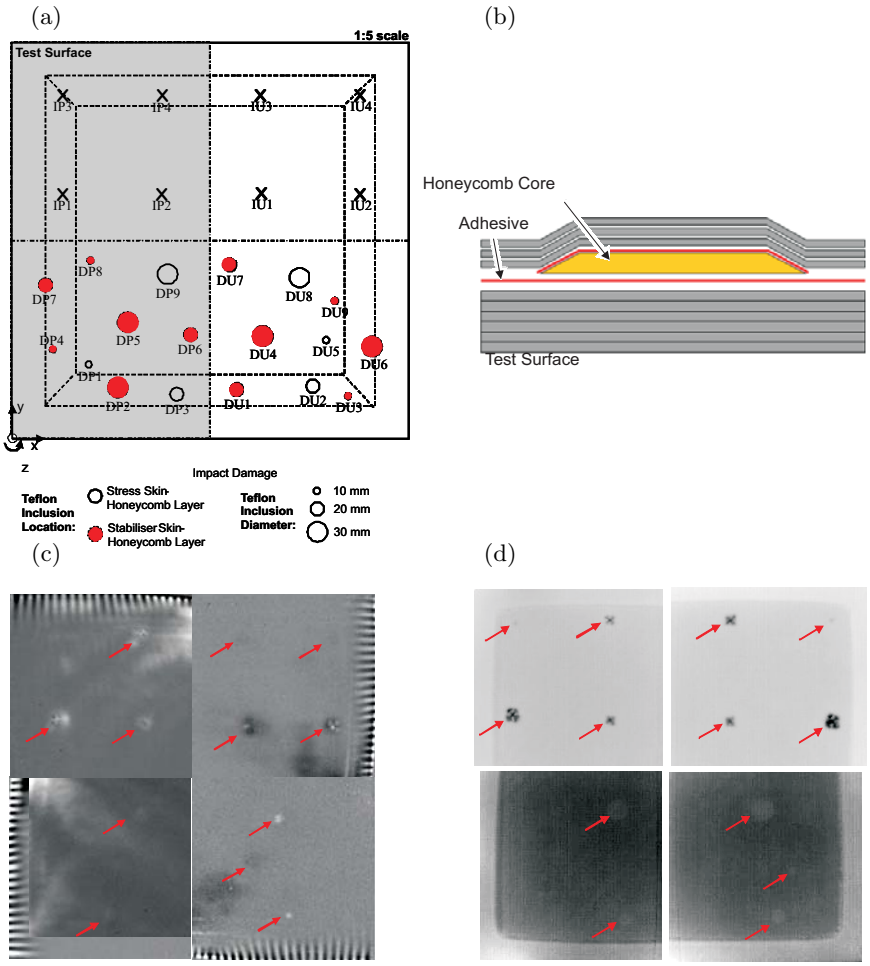

Figure 30: *(a) Damage map, (b) profile image of layup, (c) sonic and (d) flash thermographs showing the four quadrants of specimen 2A and the corresponding damage locations. (Specimen layout courtesy CRC-ACS.)*

Figure 30 shows the ST and FT results for specimen 2A and the corresponding damage map. Specimen 2A is a honeycomb reinforced panel with the reinforcement confined to the region of the panel within the outer dashed line of Figure 30(a). The area between the dashed lines corresponds to a sloping section of the honeycomb structure as shown in Figure 31. Inclusions were located between the honeycomb core and stablising skin, as well as between the honeycomb core and the stress skin, both shown in Figure 31. Inclusions were also located on the sloping edge between the honeycomb core and stabilising skin. Table 7 shows the theoretical detectability of disbonds based on the rule of thumb described in section 3.2. These results indicate that all disbonds located in the stress skin/ honeycomb layer are, in principle, detectable. Disbonds located in the stabiliser skin/ honeycomb layer, are not detectable, however 30 mm defects located in the sloping edge should be detectable and 20 mm defects in this region should be partially detectable. The thermographs indicate this to be the case with only DP1 not detected. DP2 was located using ST only. As with specimens 1A and 1B, the addition of the Cu mesh in the skin reduces the detection rate for the reasons already outlined for specimen 1B (see Figure 32).

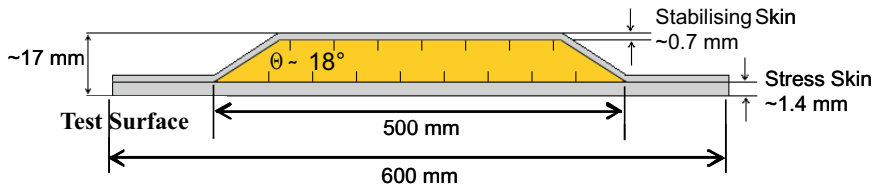

Figure 31: *Profile image of the layup of specimen 2A (courtesy CRC-ACS).*

Table 7: *Table showing minimum detectable defect size for IR thermography with respect to the Teflon disbonds in specimen 2A*

Defect size (mm)	D/2 (mm)	Depth (stress skin & HC) (D/2 $\geq$ 1.38 mm)
10	5	✓
20	10	✓
30	15	✓

'D/2' reflects the effective radius.
'Depth' indicates the depth of the embedded defect and whether it is detectable based on the empirical rule given by Maldague [14].

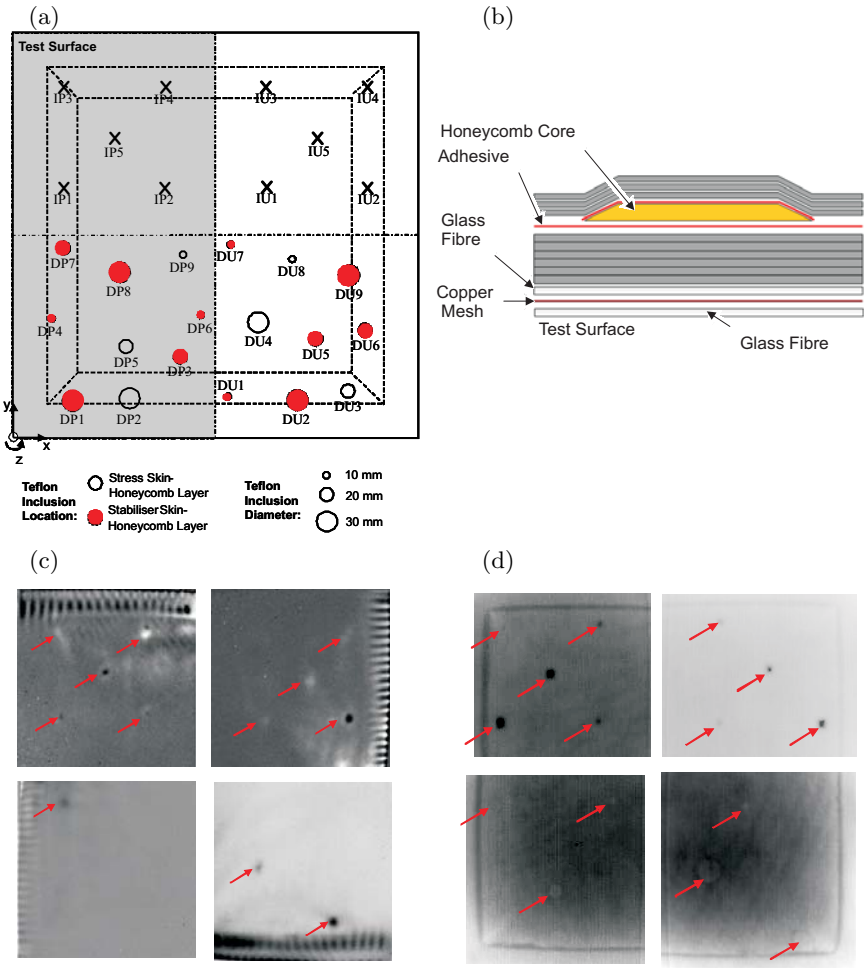

Figure 32: *(a) Damage map, (b) profile image of layup, (c) sonic and (d) flash thermographs showing the four quadrants of specimen 2B and the corresponding damage locations. (Specimen layouts courtesy CRC-ACS.)*

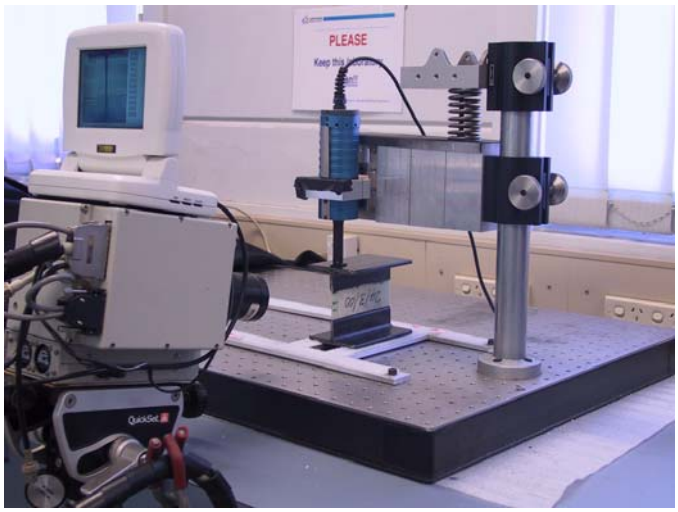

Figure 33: *Experimental setup for investigation of I-beam defects, showing thermal camera, acoustic horn and specimen.*

5 I-beam inspection: geometrically challenging structures

The increasing geometric complexity found in modern composite structures raises a number of difficult NDI challenges. One example is integrally stiffened composite panels, where stiffeners are often inaccessible and thereby difficult to inspect yet are just as prone to manufacturing flaws as more accessible panel sections. Pultruded composite I-beams are a case in point. The pultrusion process allows for the efficient manufacture of beams with high strength to weight ratio, however if the process is not carefully controlled flaws can appear in the critical web-flange junction where detection is problematic because of poor accessibility and sub-optimal defect orientation. With its use of diffuse acoustic excitation ST provides a promising basis for the inspection of this class of problem, provided camera access is available. To assess the performance of ST for this type of problem, two C/Ep I-beams were investigated. Figure 33 shows a photograph of the experimental setup for this investigation. The specimens were insonified for 10 s with the horn set to 500 W and thermal image capture at 30 Hz. Figure 34(a) shows a photograph of a typical I-beam with the two regions under investigation marked A (web) and B (the web-flange junction). In this case region A has an existing crack and region B has no visible damage.

Region A of the first I-beam inspected showed visible damage in the web and during insonification this damage was clearly observed as a region of increased heat production as shown in Figure 34(b). For this particular I-beam no damage was found in region B. Region B of the second I-beam showed some signs of cracking along the exposed surface of the flange. During insonification further internally located damage was detected. Figure 35 shows a photograph of the section under investigation (top) along with the sonic PCT_3 result (middle). The bottom image shows the sonic PCT_3 result for a reference specimen with no observable cracks.

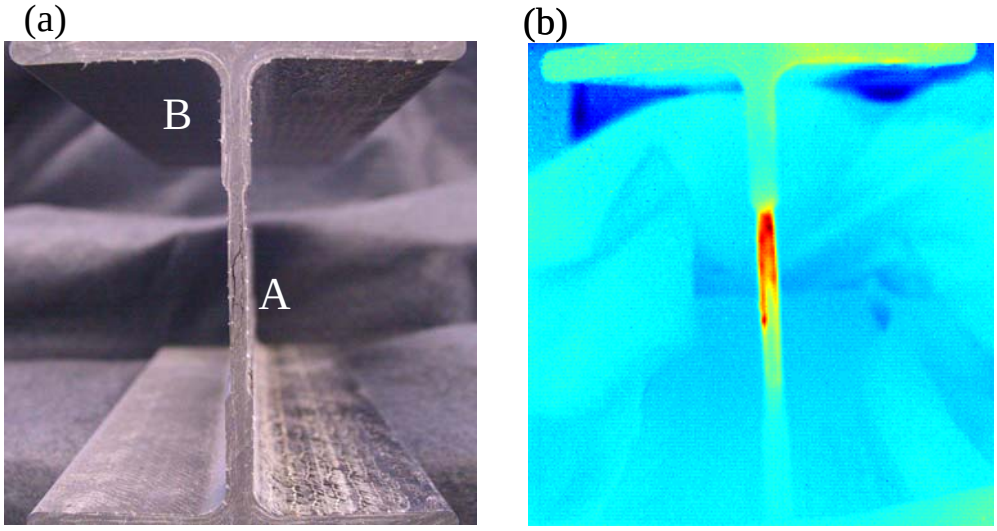

Figure 34: *(a) Photograph of I-beam showing the regions of interest, A and B, and (b) the corresponding sonic thermograph.*

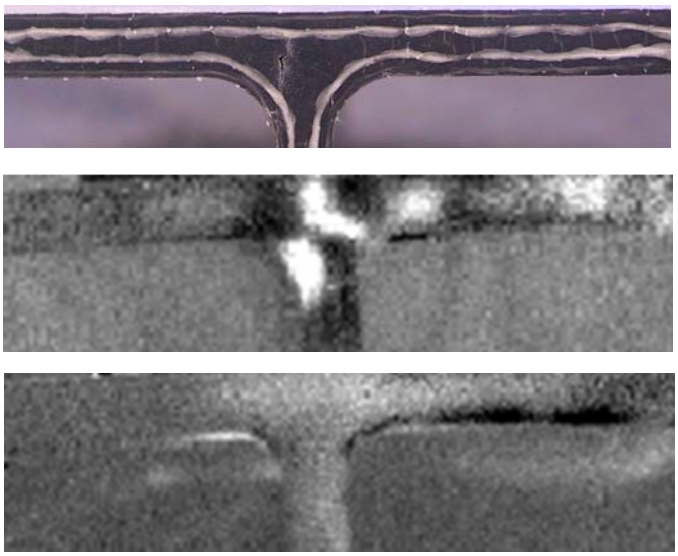

Figure 35: *Photograph of region B (top) and the sonic PCT_3 results for the damaged area of the I-beam (middle) and the reference specimen (bottom).*

6 Crack detection beneath CBRs

One of the concerns often raised about CBRs is the possibility that a patch may hinder continued inspection of the underlying damage. For instance, where crack patching merely slows the growth of an existing crack it is important to be able to monitor the crack growth after the patch is applied. There are various techniques which can be used to monitor crack growth beneath a patch. X-radiography is generally effective in this regard, however it is cumbersome to apply and harbours obvious health risks to operators. Eddy current can also be effective, however there is a limitation to the thickness of composite patch that may be accommodated given the exponential increase in geometric attenuation with probe-metal separation. In this section a demonstration is given of the effectiveness of ST in detecting cracks beneath a B/Ep repair on a specially prepared test specimen.

B/Ep repair technology was developed by DSTO as a cost effective means of restoring the structural integrity of damaged aircraft components. A highly successful application is to the F-111 lower wing skin. As part of the repair development program, generic specimens were prepared to determine the patching efficiency of B/Ep repairs used for the remediation of fatigue cracking [23]. One of the specimens used in this study is investigated here in order to examine the efficacy of ST in detecting cracks beneath a patch.

The specimen used consisted of two 2024 T3 aluminium alloy panels, each 3.14 mm thick with initial 5 mm edge notches which were pre-cracked and then repaired with unidirectional B/Ep (Textron 5521/4) patches, 7 plies (0.9 mm) thick. The two panels were joined with a 3.2 mm thick honeycomb sandwich panel, in order that: (a) the panels could be fatigue tested simultaneously, (b) bending curvature caused by the application of the patches is minimised and (c) secondary bending of the panels during tensile testing is minimised. The specimen had undergone fatigue cycling in order to grow the edge cracks to a length of 5 mm before the application of the B/Ep repair.

Figure 36 shows an image of the specimen with the dimensions of the various sub-structures indicated. The top shows the semicircular B/Ep patch and the bottom image shows a side-on view of the specimen. The edge notches in the aluminium panels are indicated, as are the four points of insonification. The specimen was painted black in order to remove any emissivity variations and was insonified for 5 s. The horn was set to 500 W and 300 frames were captured at a frame rate of 10 Hz.

Figure 37 shows the flash PPT results for sides A and B (as indicated). No indications of a defect are present. Figure 38 shows the ST raw image, PPT and PCT_2 results pertaining to sides A and B for insonification at point a and Figure 39 shows the ST raw image, PPT and PCT_2 results for insonification at point b. The differences between the two points of insonification are marked. Two distinct mode shapes are evident in the series: the horizontally banded pattern in Figure 38, and the more complex pattern shown in Figure 39. It is important to note, however, the consistency of the vertical indication extending upward from the base of the patch. This indication corresponds well to the location and length of the underlying crack. Figure 40 shows the results (both PPT and PCT) of insonification at the four different points (as indicated in Figure 37) on side A. The result suggests that defect indications may be distinguished from vibrational mode patterns by performing a cross-correlation between inspections where different mode shapes are excited (also mentioned in Section 3.7).

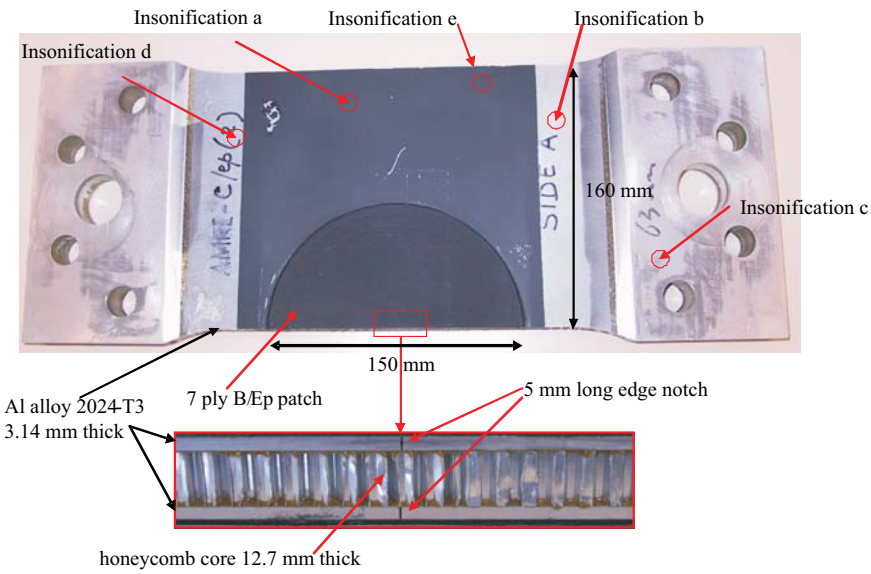

Figure 36: *Photograph of the B/Ep patched honeycomb panel showing the dimensions and insonification points.*

Figure 41 shows an example of a cross-correlation between two PCT_2 results. The two results were drawn from insonifications at points a and e, as indicated in Figure 36. The result shows the effectiveness of this simple image processing step in delineating the crack signature from the vibrational mode patterns.

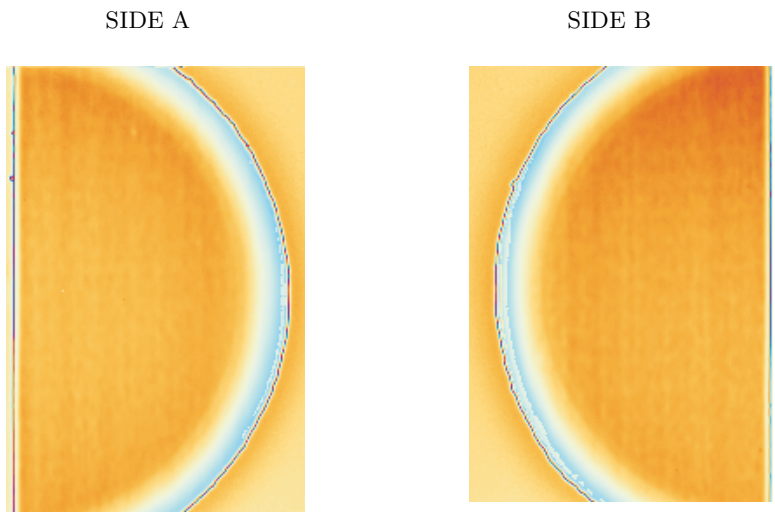

Figure 37: *FT PPT results of sides A and B of the B/Ep patched honeycomb panel.*

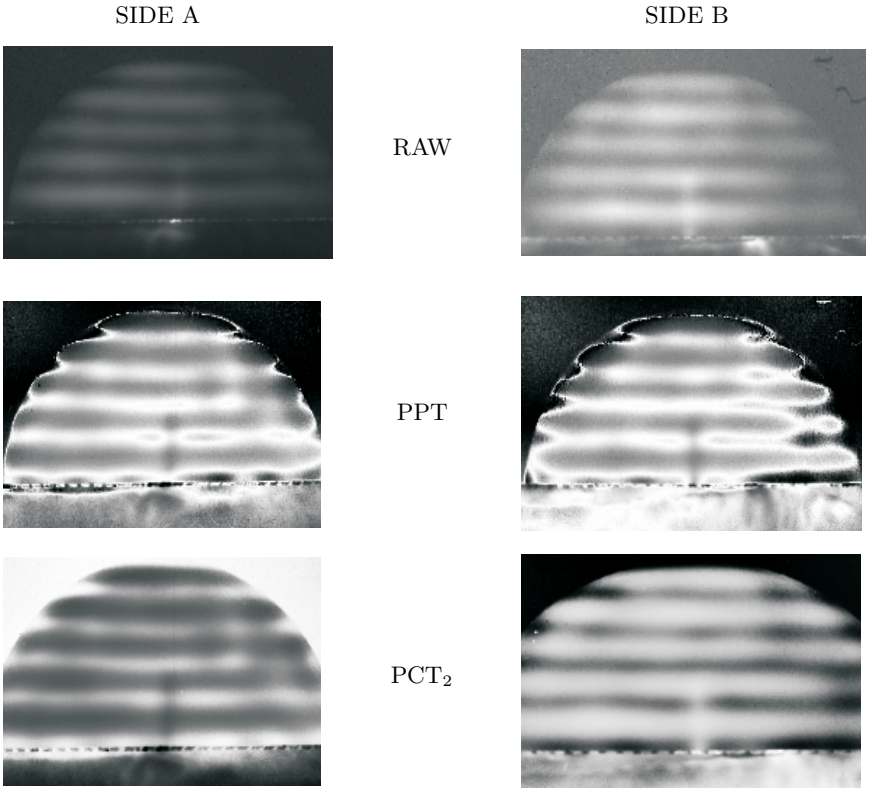

Figure 38: *ST raw, PPT and PCT$_2$ results of the B/Ep patched honeycomb panel insonified at point a (indicated in Figure 36).*

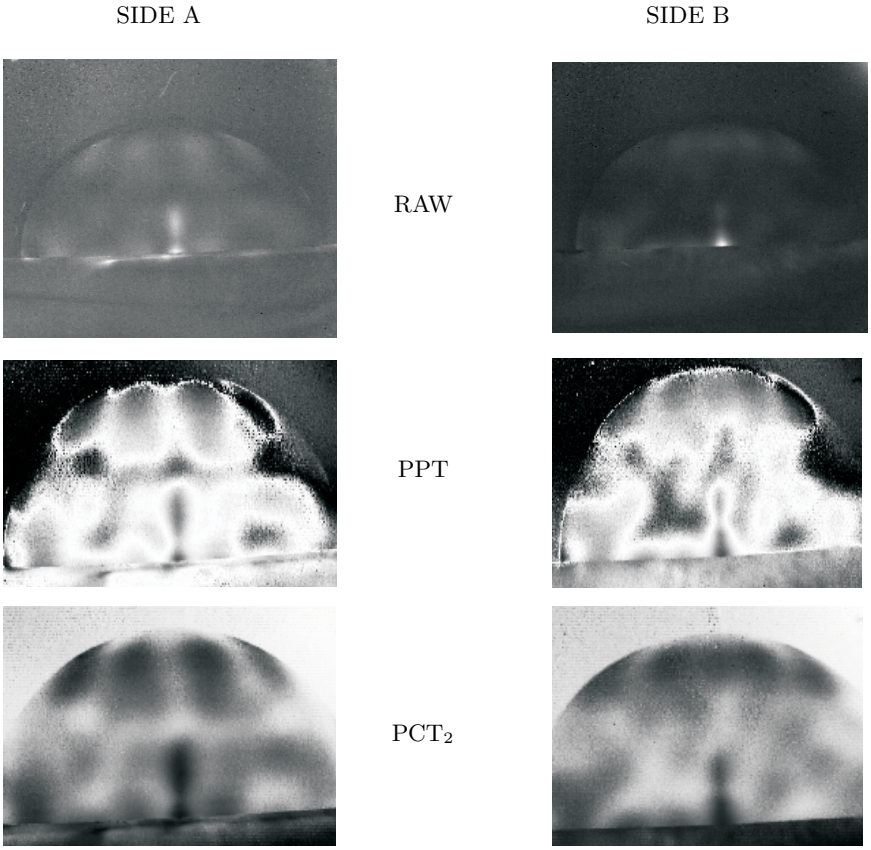

Figure 39: *ST raw, PPT and PCT$_2$ results of the B/Ep patched honeycomb panel insonified at point b (indicated in Figure 36).*

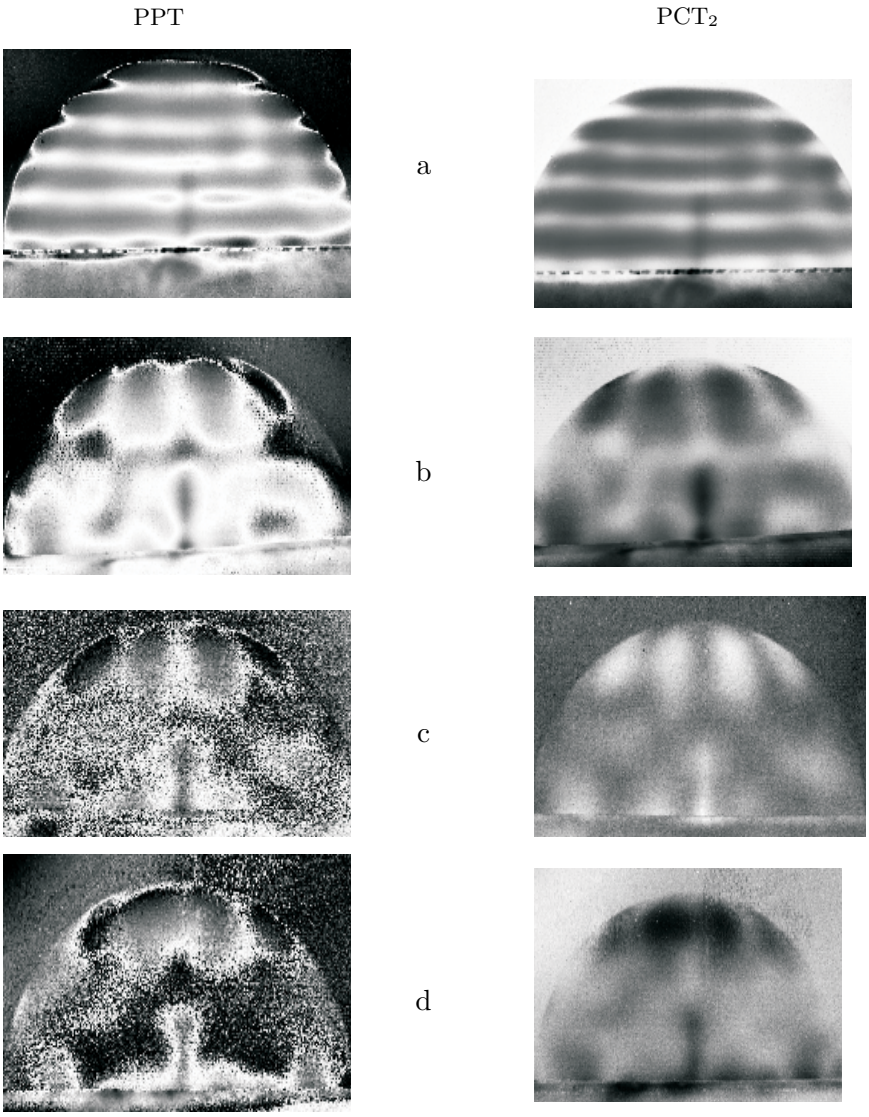

Figure 40: *ST PPT and PCT_2 results of B/Ep patched honeycomb panel insonified at four locations (a, b, c and d) on side A, as indicated, corresponding to Figure 36.*

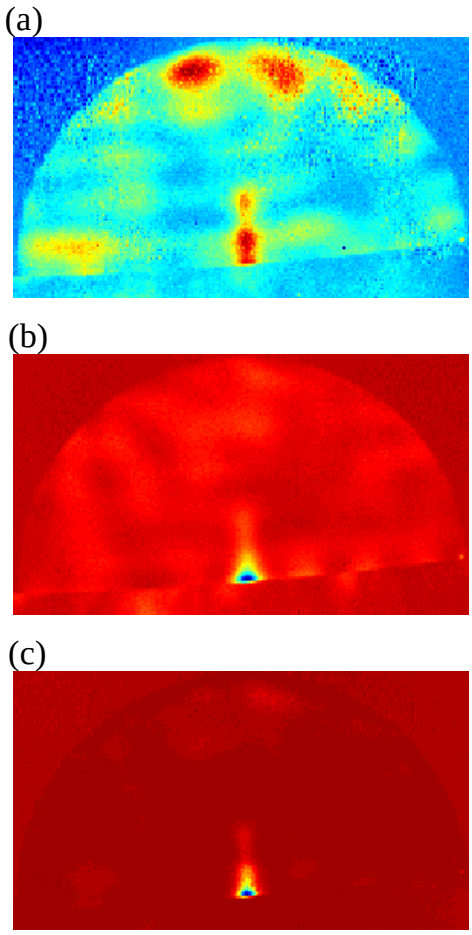

Figure 41: *(a) and (b) show the ST PCT_2 results of B/Ep patched honeycomb panel insonified on side A at locations a and e, respectively, corresponding to Figure 36. (c) is the cross-correlation result of the two PCT results.*

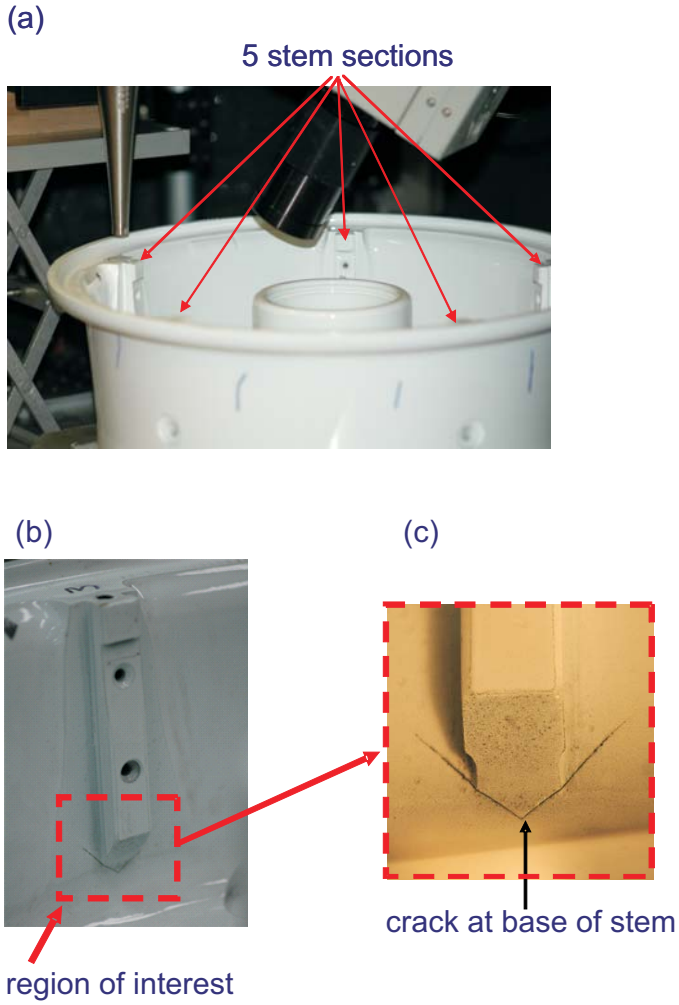

Figure 42: *Photograph of (a) F-16 main wheel rim, the five stems to be inspected are indicated, (b) one of the stems, with the region of interest highlighted by the box and (c) a close up view of the area to be inspected. For this case a visible crack is observable.*

7 Cracking in an F-16 main wheel rim

As part of the TTCP-MAT-TP5-O28 operating assignment in sonic thermography, a round robin exercise was undertaken to compare the performance of the different thermographic inspection systems used by the participating TTCP countries on a standard aircraft component [24]. A blind test was arranged of an F-16 main wheel rim sourced from the Wright Patterson Air Force Base. A photograph of the F-16 main wheel rim is shown in Figure 42(a). The rim has five stems which are susceptible to cracking, an example of which is shown in Figure 42(b). The area of interest is on the inside of the rim, at the bottom of the stem as indicated in Figure 42(c). Cracks initiate at the bottom corners of the stem (arrows) and grow outward, joining at the apex, below the centre of the stem. The crack shown in this photograph has grown through the thickness of the rim and is an extreme case. Due to the difficult geometry, a mirror was used in order to place the area of interest within the field of view of the IR camera, as shown in Figure 43.

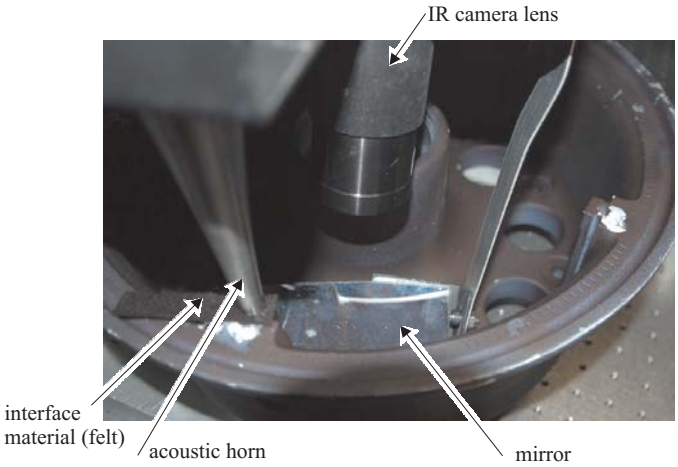

Figure 43: *Experimental setup showing painted main wheel rim with the mirror, IR camera and acoustic horn in position.*

For typical thermographic inspections, the subject is coated with a high emissivity paint in order to remove background thermal reflections which could contaminate the results. The main wheel rim arrived with a matt white surface coating and was inspected as-received and again after applying a thin coat of high emissivity water-based paint. For this inspection the application of paint improved signal quality but was not vital in rendering defects detectible.

7.1 Effect of horn tip position on IR signature

The position of the horn tip during insonification was found to have a large influence on whether or not the cracks were observable. This was of particular importance in the detection of the smaller cracks observed in stems 1 and 2, which are not visible to the naked eye. To determine the best location for the injection of acoustic energy, several areas on the main wheel rim were investigated. Due to the location of the cracks, at the bottom of the stem, the horn tip was positioned just above the main bulk of the stem shown as position 1 in Figure 44. However, no IR signal was detected at the location of the smaller non-visible cracks (Figure 45(a)). This suggests that only a small amount of energy is transmitted into the zone of the crack. The horn was repositioned on the edge of the stem, indicated by position 2 in Figure 44 and the inspection repeated. The IR signature from the smaller cracks was significantly improved. Two indications are furnished by the excitation at position 2 (Figure 45(b)). In effect, the stem serves as a wave guide directing the acoustic energy towards the cracked region.

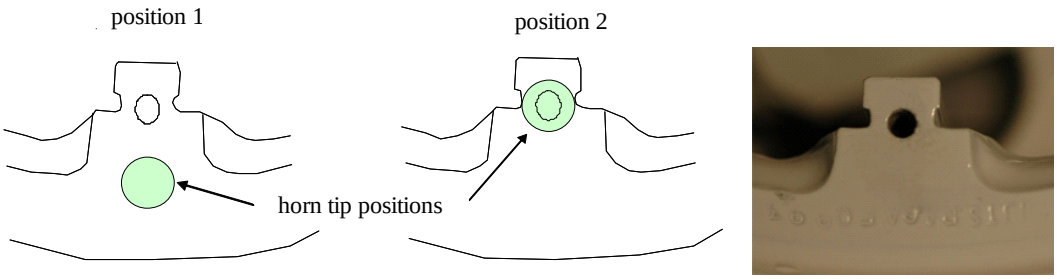

Figure 44: *Horn tip positions.*

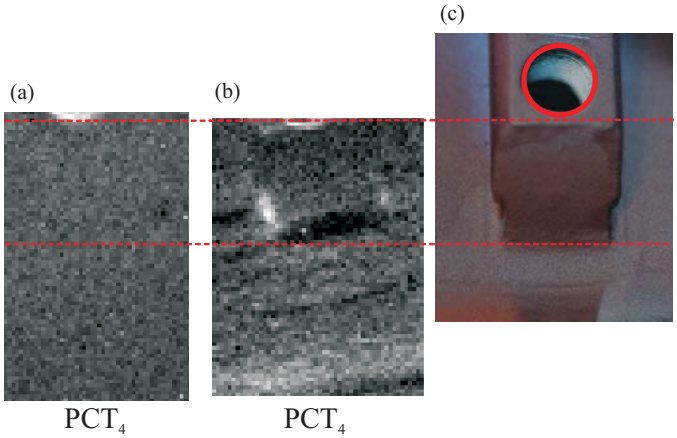

Figure 45: *PCT results corresponding to insonification positions (a) 1 and (b) 2 of stem 2. (c) shows a photograph of the region. The parallel lines are used to align the thermal images with the photograph.*

7.2 Effect of power level and insonification time on IR signature

A study on the effect of power level on the IR signature was conducted. Levels of 600 W (50% of the total available power), 840 W (70%) and 1200 W (100%) were considered. Stem 1 was made the subject of the study as this stem had cracking which was not visible. The interface material was found to disintegrate at the 1200 W (100%) level and was, therefore, not considered a useful level for routine inspection. The results, shown in Figure 46, indicated that 840 W (70%) was sufficient to obtain a clear, reliable IR signature from the cracks and had a negligible effect on the interface layer. This power level was used for all inspections of the wheel.

A sensitivity study was also undertaken on stem 1 to examine the effect of insonification time on signal quality. The results are also shown in Figure 46. Generally, an insonification time of 1-2 s was enough to produce reliable indications, however a 4 s duration was found to provide marginally stronger signals and was therefore used throughout this study.

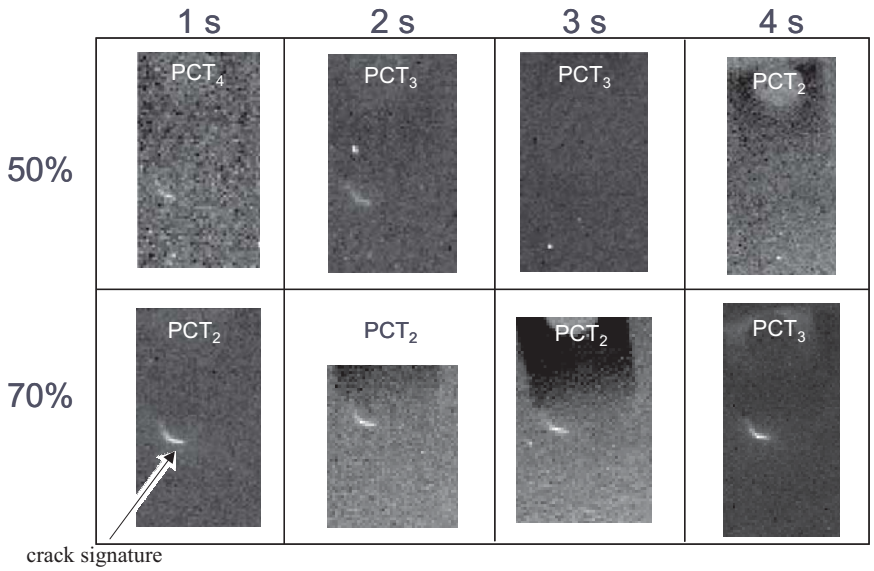

Figure 46: *PCT results for stem 1 indicating varying insonification times (1 s, 2 s, 3 s, 4 s) and power levels (50% and 70%).*

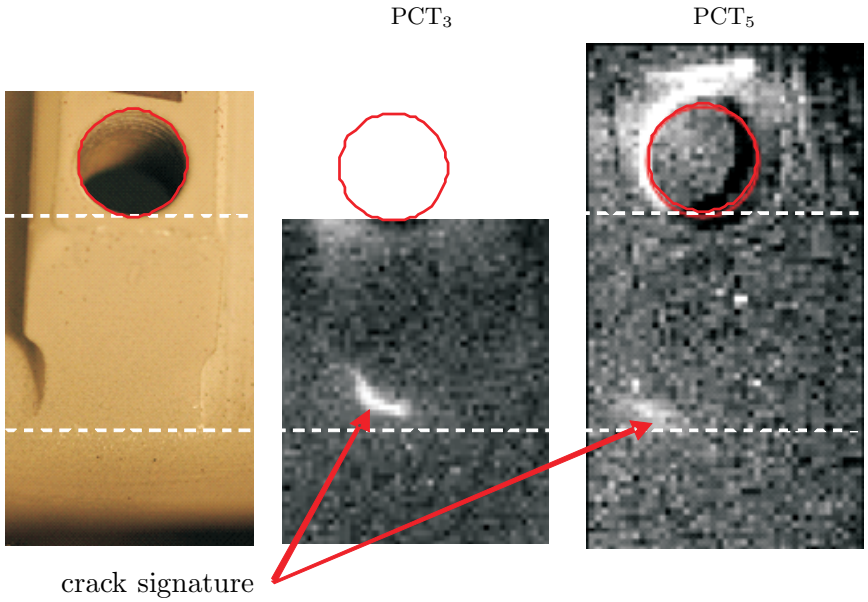

Figure 47: *Stem 1: photograph and PCT results for the painted (left) and unpainted area (right), respectively.*

7.3 Summary of results

Cracks were found only in stems 1, 2, 3 and 4. The chosen input power of 840 W equates to approximately 120 W of actual power going into the rim as measured by the horn instrumentation. An insonification time of 4 s was used. The results shown are for both the unpainted (no high emissivity paint applied) and painted (high emissivity paint applied) surfaces, as indicated.

7.3.1 Stem 1

Figure 47 shows a photograph of the area of interest and the PCT results for the painted and unpainted cases, respectively. The parallel white lines are used to align the photograph with the PCT results and the red circles indicate the position of the hole at the top of the stem. There was no visible evidence of cracking and it should be noted that any existing cracks may be masked by the white surface coating of the rim. The PCT results for the painted and unpainted cases show the thermal indication of a crack on the bottom left corner of the stem. Although the painted case shows greater definition, the unpainted case also provides evidence of the crack.

7.3.2 Stem 2

Figure 48 shows a photograph of stem 2, and the PCT results for painted and unpainted cases. Once again, no visible evidence of cracking is observed. The PCT results indicate cracking on both corners of the stem, with little difference between the painted and unpainted cases.

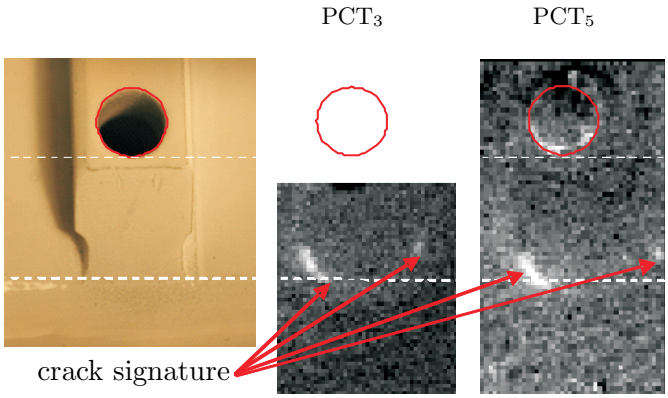

Figure 48: *Stem 2: photograph and PCT results for the painted (left) and unpainted area (right), respectively.*

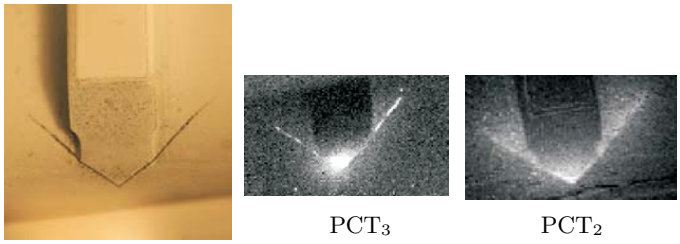

Figure 49: *Stem 3: photograph and PCT results for the painted (left) and unpainted area (right), respectively.*

7.3.3 Stem 3

Figure 49 shows stem 3, along with the painted and unpainted PCT results. This stem exhibited a large, visible crack. The crack had grown through the wall of the main wheel rim. The PCT results for both painted and unpainted cases show a substantial thermal response from the crack, as expected from a defect of this size.

7.3.4 Stem 4

Figure 50 shows a photograph of stem 4 and the PCT results for the painted and unpainted cases. This stem had no visible cracking. For the painted case insonification provided a strong indication of cracking at both corners of the bottom of the stem. Although a thermal indication also appears for the unpainted results, it is not as well defined as for the painted results.

7.3.5 Stem 5

Figure 51 shows the photograph of stem 5 and the PCT results for the painted and unpainted cases. This stem had no visible cracking. The PCT results gives no indication of cracking at the corners of the stem.

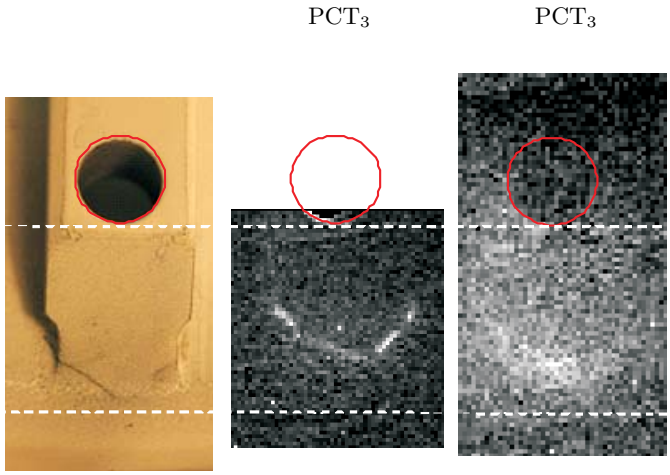

Figure 50: *Stem 4: photograph and PCT results for the painted (left) and unpainted area (right), respectively.*

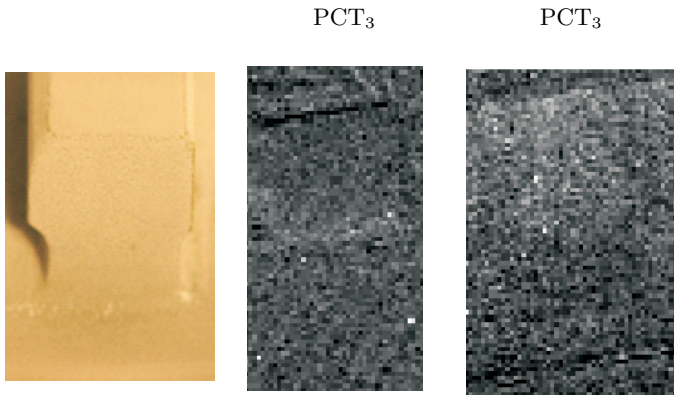

Figure 51: *Stem 5: photograph and PCT results for the painted (left) and unpainted area (right), respectively.*

8 General Discussion and Conclusions

The inspections described in this report confirm that ST is an effective technique for the detection of a range of structural defects in aircraft components and, in particular cases, can outperform other methods of inspection like FT and ultrasonic testing (UT), i.e. for kissing bonds in the Mirage and F-111 CBR applications. Consequently, ST could provide a useful NDI capability for the ADF. Its application is not straightforward and the user needs to be aware of several important issues before considering its application to an inspection problem, whether in the laboratory or a service environment. Some of these issues are discussed in the following paragraphs.

Laboratory work done by the DSTO and described in this report has shown that the position of the acoustic horn on the sample has a large influence on the outcome of an ST inspection. For example, in the F-16 wheel inspection described in section 7 a relatively small adjustment in the position of the horn proved critical in detecting the crack. The reason this occurred was that the adjustment in horn position led to the excitation of a mode of vibration (standing-wave field) that was more conducive to the generation of frictional heating at the crack. Predicting a priori the modes that will be excited in any given structural component is difficult. As briefly discussed in section 2.1 the acoustic horn is often a poor acoustic impedance match to the material under test and can therefore produce a broad excitation spectrum (itself difficult to predict), which gives rise to a large number of possible modes of vibration. Consequently, where an inspection fails to reveal a structural defect it would be prudent to consider alternative horn positions to ensure that as many modes of vibration are excited as possible. In addition, such an approach offers an effective way of reducing the impact of parasitic thermal signatures produced by anelastic heating (see section 6).

In terms of field application, the method poses other challenges. Good acoustic coupling between the probe and the sample is needed for an efficient transfer of acoustic energy. Previous work by the DSTO [5] has shown that a thin layer of interface material placed between the probe and the component under inspection can greatly improve energy transfer and therefore increases the likelihood of detecting a structural flaw. Importantly, such an interface layer also protects the surface from fretting damage during insonification. In addition, previous DSTO work has confirmed that a compressive pre-load applied to the horn during the insonification process significantly improves energy transfer to the component. In the DSTO system, a rig was developed to allow a controlled force to be applied during inspection (i.e. the spring in Figure 1). It is likely that a similar approach could be developed for a field-inspection, however this would depend on the particular circumstances of the application and whether sufficient access for the required equipment is available. Obviously, this issue would need to be considered in assessing the feasibility of ST for a particular inspection problem.

It has been reported elsewhere [7] that NDI standards used to evaluate other NDI approaches like UT may not be appropriate for thermographic inspection techniques. This is an important consideration for ST since one of the most promising applications of the technique is to the detection of kissing bonds, a form of damage that is difficult to simulate. Kissing bonds are often simulated by embedding Teflon film during the manufacture of a composite component, whether a laminate or a CBR. Teflon, however, has a low coefficient

of friction which restricts heat production at the insert. Teflon inserts are still able to be detected using ST (see Figure 3, 28–30, 32) which suggests that some frictional heating may still occur but it is also possible that part of the heating stems from anelastic heating caused by a stress concentration at the insert. Other approaches at creating an artificial defect have been tried, including contaminating the composite lay-up with Vaseline as well as introducing an air-gap between plies. Like Teflon inserts, these types of manufactured defects seldom provide thermal indications comparable to those produced by real defects in aircraft structure (see Figures 9-10). Work is currently underway by the DSTO to develop more representative thermographic NDI standards for kissing bonds and delaminations.

The recent acquisition of MRH-90 and Tiger ARH helicopters by the ADF introduces another consideration for ST and other NDI techniques. The outer composite skin of the airframe of these helicopters contains an electromagnetic shielding (EMS) mesh made from copper. This mesh affords lightning strike protection for the aircraft and is therefore designed to efficiently conduct electrical current, and, consequently also heat. The effect on ST and FT of a high conductivity layer near the inspection surface is to attenuate and laterally smear any thermal signature stemming from a structural flaw beneath the mesh. Preliminary inspections done by the DSTO on structure containing this type of mesh appear to confirm this (see Figures 10, 29, 32). Further work is now being done at the DSTO to quantify the effect of the mesh on both ST and FT inspections.

One of the concerns held by the DSTO in its early work on ST was that the intense acoustic excitation applied to a component may in fact grow an existing structural defect. Vibrational modes are known to drive crack propagation in aircraft structures (i.e. acoustic fatigue in metallic structure) and it was thought that a similar mechanism could occur in the context of an ST inspection. An experimental study was done by the DSTO to examine this possibility [25]. It was considered that a thin metallic structure with an existing fatigue crack would be most prone to the effect so the study focused on crack growth in thin aluminium test coupons. The study found that periodic ST inspection had no statistically significant impact on the rate of crack growth in these samples. Given that composite materials have a higher resistance to fatigue than metals it is surmised that ST inspection would not have an adverse impact on structural defects in composite components.

9 Acknowledgements

The authors would like to acknowledge David Rowlands for his technical support, Sami Weinberg for his software support, Andrew Rider for the Mirage III tap testing, BaNDI-coot and pull out test results and Sue Bowles for the C-scan result in Section 3.6.

References

1. R.B. Mignogna, R.E. Green Jr, J.C. Duke Jr, E.G. Henneke II, and K.L. Reifsnider. Thermographic investigation of high-power ultrasonic heating in materials. *Ultrasonics*, pages 159–163, 1981.

2. R.B. Mignogna and R.E. Green Jr. Effects of high frequency loading on materials. *Ultrasonic Fatigue*, pages 63–85, 1982.

3. L.H. Tenek and E.G. Henneke II. Flaw dynamics and vibrothermographic-thermoelastic NDE of advanced composite materials. *Proceedings of Thermosense XIII*, 1467:252–263, 1991.

4. Th. Zweschper, A. Dillenz, and G. Busse. Ultrasound lock-in thermography- a defect-selective NDT method for the inspection of aerospace components. *Insight*, 43(3 March):173–179, 2001.

5. K.A. Tsoi, K. Yousif, I. Powlesland, and N. Rajic. Optimisation of sonic thermographic inspection. In *SPIE, Smart Structures/NDE: Nondestructive Characterization for Composite Materials, Aerospace Engineering, Civil Infrastructure, and Homeland Security III*, volume 7294, San Diego, 2009.

6. I. Perez and W.R. Davis. Optimizing the thermosonics signal. *Review of Quantitative Nondestructive Evaluation*, 22, 2003.

7. N. Rajic and D. Rowlands. The rapid detection of structural flaws in the MRH90 helicopter using infrared thermography - a field demonstration and business case. Technical Report DSTO-TR-2467, Defence Science and Technology Organisation, Australia, 2010.

8. X. Maldague and S. Marinetti. Pulse phase infrared thermography. *J. Appl. Phys.*, 79:2694–2698, 1996.

9. N. Rajic. Principal component thermography. Technical Report DSTO-TR-1298, Defence Science and Technology Organisation, Australia, 2002.

10. D.P. Roach and C.M. Scala. Non-destructive evaluation and quality control for bonded composite repair of metallic structures. In L.R.F. Rose A.A. Baker and R. Jones, editors, *Advances in the Bonded Composite Repairs of Metallic Aircraft Structure*, pages 659–726. Elsevier Science Ltd, 2002.

11. T. Kundu, A. Maji, T. Ghosh, and K. Maslov. Detection of kissing bonds by Lamb waves. *Ultrasonics*, 35:573–580, 1998.

12. C.J. Brotherhood, B.W. Drinkwater, and F.J. Guild. The effect of compressive loading on the ultrasonic detectability of kissing bonds in adhesive joints. *Journal of Nondestructive evaluation*, 21(3):95–104, 2002.

13. P.B. Nagy. Ultrasonic detection of kissing bonds at adhesive interfaces. *J. Adhesion Sci. Technol.*, 5(8):619–630, 1991.

14. X. Maldague, T.S. Jones, H. Kaplan, S. Marinetti, and M. Prystay. Fundamentals of infrared and thermal testing. In X.P.V. Maldague, editor, *Infrared and thermal testing*, volume 3, page 43. American Society for Nondestructive Testing, 3 edition, 2001.

15. S.C. Rosalie. *Lamb waves tomography for damage detection in plate-like structures.* PhD thesis, 2006.

16. M. Heller and R. Kaye. Shape optimisation for bonded repairs. In L.R.F. Rose A.A. Baker and R. Jones, editors, *Advances in the Bonded Composite Repairs of Metallic Aircraft Structure*, pages 269–315. Elsevier Science Ltd, 2002.

17. S. Weller and K. Walker. Revised durability and damage tolerance assessment of RAAF F-111C lower wing skin regions around FASS 226 and 281. Technical report, Defence Science and Technology Organisation, Australia, June 2002 2002.

18. P. Chalkley and R. Geddes. Service history of the F-111 wing pivot fitting upper surface boron/epoxy doublers. Technical Report DSTO-TN-0168, 1998.

19. A. Rider. Air Vehicles Division, Defence Science and Technology Organisation, Australia. Private communication, 2006.

20. CSIRO. http://www.csiro.au/science/bandicoot-rapid-inspection-system.html, 2011.

21. S.C. Galea and W.K. Chiu. The effect of multiple impact damage on the residual compressive strength of composite structures. *IJCrash*, 1(3):305–313, 1996.

22. T.J. Van Blaricum, P. Bates, and R. Jones. An experimental investigation into the effect of impact damage on the compressive strength of step lap joints. *Eng. Frac. Mech.*, 32(5):667–674, 1989.

23. A.A. Baker. Boron/epoxy patching efficiency studies. In A.A. Baker, L.R.F. Rose, and R. Jones, editors, *Advances in the Bonded Composite Repairs of Metallic Aircraft Structure*, pages 375–397. Elsevier Science Ltd, 2002.

24. I. Perez and W.R. Davis. Development of sonic thermography as a new wide area NDE technique. Technical Report TTCP/MAT-TP-5/3/2008, 2008.

25. K.A. Tsoi and N. Rajic. Effects of sonic thermographic inspection on fatigue crack growth in an al alloy. Technical Report DSTO-TN-0584, Defence Science and Technology Organisation, Australia, 2004.

Page classification: UNCLASSIFIED

DEFENCE SCIENCE AND TECHNOLOGY ORGANISATION DOCUMENT CONTROL DATA				1. CAVEAT/PRIVACY MARKING
2. TITLE Non-destructive Evaluation of Aircraft Structural Components and Composite Materials at DSTO Using Sonic Thermography			3. SECURITY CLASSIFICATION Document (U) Title (U) Abstract (U)	
4. AUTHORS Kelly A. Tsoi and Nik Rajic			5. CORPORATE AUTHOR Defence Science and Technology Organisation 506 Lorimer St, Fishermans Bend, Victoria 3207, Australia	
6a. DSTO NUMBER DSTO–TN–0986	6b. AR NUMBER AR-014-921		6c. TYPE OF REPORT Technical Note	7. DOCUMENT DATE February 2011
8. FILE NUMBER M1/9/1338	9. TASK NUMBER DERP 07/250	10. TASK SPONSOR CDS	11. No. OF PAGES 55	12. No. OF REFS 25
13. URL OF ELECTRONIC VERSION `http://www.dsto.defence.gov.au/publications/scientific.php`			14. RELEASE AUTHORITY Chief, Air Vehicles Division	

15. SECONDARY RELEASE STATEMENT OF THIS DOCUMENT

Approved for Public Release

OVERSEAS ENQUIRIES OUTSIDE STATED LIMITATIONS SHOULD BE REFERRED THROUGH DOCUMENT EXCHANGE, PO BOX 1500, EDINBURGH, SOUTH AUSTRALIA 5111

16. DELIBERATE ANNOUNCEMENT

No Limitations

17. CITATION IN OTHER DOCUMENTS

No Limitations

18. DSTO RESEARCH LIBRARY THESAURUS

Nondestructive tests, thermography, fatigue tests, crack propagation, Aluminum alloys, acoustics

19. ABSTRACT

This report outlines the results of a series of non-destructive evaluations using sonic thermography. It examines the detection of closed cracks, delaminations, impact damage and other defects in a variety of structural components and composite materials used in aircraft structures. The results confirm the efficacy of the technique and highlight its potential to fill some of the capability gaps that currently exist in relation to challenging non-destructive inspection problems.

Page classification: UNCLASSIFIED